THE MOSDEF SURVEY: AGN MULTI-WAVELENGTH IDENTIFICATION, SELECTION BIASES, AND HOST GALAXY PROPERTIES

Mojegan Azadi[1], Alison L. Coil[1], James Aird[2], Naveen Reddy[3], Alice Shapley[4], William R. Freeman[3], Mariska Kriek[5], Gene C. K. Leung[1], Bahram Mobasher[3], Sedona H. Price[5], Ryan L. Sanders[4], Irene Shivaei[3], and Brian Siana[3]

[1] Center for Astrophysics and Space Sciences, Department of Physics, University of California, 9500 Gilman Drive, La Jolla, San Diego, CA 92093, USA
[2] Institute of Astronomy, University of Cambridge, Madingley Road, Cambridge CB3 0HA, UK
[3] Department of Physics and Astronomy, University of California, Riverside, 900 University Avenue, Riverside, CA, 92521, USA
[4] Department of Physics and Astronomy, University of California, Los Angeles, 430 Portola Plaza, Los Angeles, CA 90095, USA
[5] Astronomy Department, University of California at Berkeley, Berkeley, CA 94720, USA

ABSTRACT

We present results from the MOSFIRE Deep Evolution Field (MOSDEF) survey on the identification, selection biases, and host galaxy properties of 55 X-ray, IR, and optically selected active galactic nuclei (AGNs) at $1.4 < z < 3.8$. We obtain rest-frame optical spectra of galaxies and AGNs and use the BPT diagram to identify optical AGNs. We examine the uniqueness and overlap of the AGNs identified at different wavelengths. There is a strong bias against identifying AGNs at any wavelength in low-mass galaxies, and an additional bias against identifying IR AGNs in the most massive galaxies. AGN hosts span a wide range of star formation rates (SFRs), similar to inactive galaxies once stellar mass selection effects are accounted for. However, we find (at $\sim$2–3σ significance) that IR AGNs are in less dusty galaxies with relatively higher SFR and optical AGNs in dusty galaxies with relatively lower SFR. X-ray AGN selection does not display a bias with host galaxy SFR. These results are consistent with those from larger studies at lower redshifts. Within star-forming galaxies, once selection biases are accounted for, we find AGNs in galaxies with similar physical properties as inactive galaxies, with no evidence for AGN activity in particular types of galaxies. This is consistent with AGNs being fueled stochastically in any star-forming host galaxy. We do not detect a significant correlation between SFR and AGN luminosity for individual AGN hosts, which may indicate the timescale difference between the growth of galaxies and their supermassive black holes.

Key words: galaxies: active – galaxies: evolution – galaxies: high-redshift – galaxies: Seyfert

1. INTRODUCTION

Active galactic nuclei (AGNs) are the result of accretion of gas and dust onto the supermassive black holes (SMBHs) at the centers of galaxies, and have been investigated in numerous studies over the past two decades (for a recent review of black hole growth see Alexander & Hickox 2012). Various observational results have shown evidence for a global connection between the growth of SMBHs and the galaxies in which they live. For example, the relatively tight correlation between the SMBH mass and the bulge stellar mass (e.g., Magorrian et al. 1998) or bulge velocity dispersion (e.g., Ferrarese & Merritt 2000; Gebhardt et al. 2000; Kormendy et al. 2011) supports the idea of a close connection between the growth of SMBHs and their host galaxies. In addition, the similar evolution of the SMBH accretion rate density and star formation rate (SFR) density with redshift indicates a global connection between AGN activity and the formation of stars in galaxies (e.g., Boyle & Terlevich 1998; Silverman et al. 2008; Aird et al. 2010; Assef et al. 2011). However, the details of the coeval growth of galaxies and their SMBHs are not well understood.

Accretion onto SMBHs releases a tremendous amount of energy, and thus AGNs produce significant radiation at X-ray, ultraviolet (UV), optical, infrared (IR), and radio wavelengths. Different studies have used emission at one or more of these wavelengths to identify AGNs and subsequently investigate the nature of their host galaxies (e.g., Kauffmann et al. 2003; Goulding & Alexander 2009; Kauffmann & Heckman 2009;

Aird et al. 2012; Mendez et al. 2013; Azadi et al. 2015; Cowley et al. 2016; Harrison et al. 2016).

One of the most reliable methods of identifying AGNs is X-ray imaging from deep surveys carried out with the *XMM-Newton*, *Chandra* and, more recently, *NuSTAR* telescopes (for a recent review see Brandt & Alexander 2015). The X-ray emission from AGNs is strong enough to outshine the X-ray light associated with intense star formation (SF) activity and penetrate regions with high hydrogen column density (up to $N_H \approx 10^{23-24}\ cm^{-2}$). Thus, hard-band (2–10 keV) X-ray selection is sensitive to both unabsorbed and moderately absorbed AGNs, and is relatively unaffected by host galaxy dilution.

However, X-ray emission is strongly absorbed by Compton-thick regions with hydrogen column density of $N_H > 1.5 \times 10^{24}\ cm^{-2}$ (e.g., Della Ceca et al. 2008; Comastri et al. 2011; Brightman et al. 2014). Studies of local and non-local AGN samples estimate that 10%–50% of the entire AGN population are Compton thick (e.g., Akylas & Georgantopoulos 2009; Vignali et al. 2010; Alexander et al. 2011; Buchner et al. 2015; Lanzuisi et al. 2015), demonstrating that such heavily obscured sources represent a sizable fraction of the full AGN population. Also X-ray identification is not successful in identifying less powerful AGNs that are accreting at very low rates (e.g., Gilli et al. 2007; Aird et al. 2012) or AGNs residing in less massive galaxies (e.g., Mendez et al. 2013).

For heavily obscured AGNs that cannot be recovered by X-ray imaging, identification at other wavelengths may be used. The obscuring dust absorbs the UV and optical radiation

from the central engine and re-emits thermal radiation at mid-IR (MIR) wavelengths (e.g., Neugebauer et al. 1979; Rieke & Lebofsky 1981). AGNs can thus show a red power-law at MIR wavelengths in their spectral energy distributions (SEDs) (e.g., Alonso-Herrero et al. 2006; Donley et al. 2007, 2012; Mateos et al. 2012), which can be identified with imaging from the Infrared Array Camera (IRAC; Fazio et al. 2004) on *Spitzer* or with the *Wide-field Infrared Survey Explorer* (Wright et al. 2010). Dust heated by AGNs is warmer than dust heated by SF (e.g., Donley et al. 2012), which allows AGNs to be distinguished from normal star-forming galaxies at these wavelengths.

Different selection techniques have been proposed to separate AGNs from the galaxy population in MIR color–color space (e.g., Lacy et al. 2004; Stern et al. 2005; Assef et al. 2010; Donley et al. 2012; Mateos et al. 2012; Messias et al. 2012). These methods can identify heavily obscured X-ray and optical AGNs (e.g., Daddi et al. 2007; Fiore et al. 2008) as well as luminous AGNs, regardless of the obscuration and viewing angle (e.g., Hao et al. 2011). However, studies show that samples of AGNs based on any of these IR selection techniques suffer from selection biases such that they mainly identify luminous AGNs (e.g., Mendez et al. 2013).

AGNs also produce significant radiation at optical wavelengths. Broad optical emission lines (FWHM $> 2000\,\mathrm{km\,s^{-1}}$) in unobscured AGNs and narrow optical emission lines in obscured AGNs, which arise from gas located several hundred parsecs away from the SMBH (therefore suffering only from moderate obscuration (e.g., Keel et al. 1994; Kauffmann et al. 2003)), can provide detailed information about the central SMBH. At low redshifts, optical diagnostics such as the "BPT diagram" (e.g., Baldwin et al. 1981), which shows the optical emission line ratios of [N II]/Hα versus [O III]/Hβ, have been widely used to identify AGNs. Various studies based on Sloan Digital Sky Survey (SDSS) data indicate that AGNs and star-forming galaxies form distinct sequences on the BPT diagram with some overlap (e.g., Kauffmann et al. 2003; Kewley et al. 2006; Kauffmann & Heckman 2009; for a recent review see Heckman & Best 2014). One of the greatest advantages of this technique is that it can identify less powerful AGNs with low accretion rates that might be obscured at other wavelengths.

Despite its advantages, there are various issues with the BPT diagnostics. The narrow optical emission lines can suffer from significant extinction due to the dust in the galaxy. Also at higher redshifts it is more difficult to detect the required lines for the BPT diagram at high signal-to-noise ratio (as the optical emission lines shift to the near-IR wavelengths where the terrestrial background is higher). With AGNs and SF both being sources of optical emission lines, disentangling the contributions from each of these phenomena can be another challenge (e.g., Kauffmann & Heckman 2009; Wild et al. 2010; Tanaka 2012). Furthermore, using the BPT diagram at higher redshifts may require re-calibration of the lines separating AGNs from the star-forming sequence (e.g., Coil et al. 2015; Shapley et al. 2015).

The selection biases in each identification method indicate that using a single waveband cannot recover the full population of AGNs (e.g., Hickox et al. 2009; Juneau et al. 2011; Mendez et al. 2013; Trump et al. 2013; Goulding et al. 2014). Many studies have investigated properties of AGN host galaxies using multi-wavelength data at low and moderate redshifts

(e.g., Klesman & Sarajedini 2012; Mendez et al. 2013; Goulding et al. 2014; Sartori et al. 2015). To obtain a better understanding of the properties of AGN host galaxies requires detailed information at $z \sim 1$–3, the epoch of peak of AGN activity; however, current samples at these redshifts are relatively small.

Studying the host galaxies of AGNs—revealing the types of galaxies that tend to host them—can provide important insights into the physical mechanisms that trigger AGN activity. Furthermore, we can assess whether AGNs appear to have an impact on the galaxies that they live in, altering their properties compared to the overall galaxy population. Numerous studies have investigated the position of AGNs in the color–magnitude diagram, as well as SF activity, stellar mass, stellar age, or colors of AGN host galaxies at different redshifts to investigate the impact of AGN activity on their host galaxies (e.g., Kauffmann & Heckman 2009; Schawinski et al. 2011; Aird et al. 2012; Rosario et al. 2013, 2015; Georgakakis et al. 2014; Hernán-Caballero et al. 2014). It is known that galaxies in the optical color–magnitude diagram show a strong bimodal behavior and can generally be divided into two populations: the blue cloud of star-forming galaxies and the red sequence with mainly passive, quiescent galaxies (e.g., Bell et al. 2003; Blanton et al. 2003; Baldry et al. 2004). Early studies found that the majority of AGNs lie on the red sequence (e.g., Nandra et al. 2007; Hickox et al. 2009) and concluded that AGN feedback may be shutting down SF in their host galaxies. More recent studies, however, highlight the importance of stellar-mass-dependent selection effects (e.g., Silverman et al. 2009; Cardamone et al. 2010; Xue et al. 2010; Aird et al. 2012; Hainline et al. 2012). In fact, most of these studies find that in a sample with matched stellar mass host galaxies, AGNs are equally likely to be found in any host population.

Using far-IR (FIR) and sub-mm measurements from *Herschel* and *ALMA*, many recent studies find that AGNs predominantly live in star-forming galaxies (e.g., Harrison et al. 2012; Mullaney et al. 2012, 2015; Santini et al. 2012; Rosario et al. 2013). However, *Herschel* observations are biased toward FIR bright galaxies. Aird et al. (2012) and Azadi et al. (2015) use samples of moderate luminosity AGNs and stellar mass complete galaxies from the PRIMUS redshift survey to show that AGNs reside in both the quiescent and star-forming galaxy populations, although galaxies that are forming stars are 2–3 times more likely to host an AGN. While these studies find evidence of enhanced SF activity in AGN hosts (compared to inactive galaxies with a similar mass distribution), uncertainties in estimates of SFR (e.g., due to the depth of the observations, the effects of dust reddening, or corrections for AGN contamination), as well as the various selection biases inherent to AGN samples, limit our understanding of the connection between black hole growth and the growth of galaxies, especially at high redshifts.

A number of studies have investigated whether there is a correlation between the SFR and AGN activity in individual galaxies (see, e.g., Azadi et al. 2015, and references therein). Tracking SF activity only in circumnuclear regions ($r < 1$ kpc), Diamond-Stanic & Rieke (2012) find evidence of a correlation between the luminosity of nearby Seyferts and their nuclear SF and conclude that these process are related in the very central regions of galaxies (see also LaMassa et al. 2013). Tracking galaxy-wide SF, studies of moderate luminosity AGNs

typically find no significant correlation between SFR and AGN activity (e.g., Mullaney et al. 2012; Rosario et al. 2012; Azadi et al. 2015; Stanley et al. 2015), while studies of the most luminous AGNs find a positive trend that could be driven by major mergers (e.g., Rosario et al. 2012; Dai et al. 2015; Bernhard et al. 2016). However, rapid variability in the AGN luminosity can result in scatter, consequently washing out the intrinsic correlation between AGN luminosity and SFR. Therefore considering the average AGN luminosity for samples of galaxies of a fixed SFR, instead of the luminosities of individual AGNs, may be more appropriate for exploring the relationships between AGN activity and SF (e.g., Hickox et al. 2014). In fact, studies investigating average AGN luminosity in bins of SFR find a positive correlation between AGN luminosity and SFR (e.g., Chen et al. 2013; Azadi et al. 2015; Dai et al. 2015).

Due to the reliability of X-ray AGN identification, the majority of the studies discussed above use only X-ray imaging to identify AGNs and subsequently assess the properties of their host galaxies using multi-wavelength data. As noted above, MIR imaging and optical rest-frame spectroscopy can also identify AGNs that may be obscured at other wavelengths. Optical spectra in particular can also provide detailed information about the gas, dust and stellar populations of the AGN host galaxies. Until recently such detailed information has been only available at low redshifts, but with the advent of multi-object near-infrared (NIR) spectrographs such as KMOS (Sharples et al. 2013) and MOSFIRE (McLean et al. 2012), this information can be obtained at high redshift as well (e.g., Trump et al. 2013; Genzel et al. 2014; Coil et al. 2015; Harrison et al. 2016).

In this paper we use rest-frame optical spectra from the MOSFIRE Deep Evolution Field (MOSDEF) survey (Kriek et al. 2015) taken with the MOSFIRE multi-object NIR spectrograph on the Keck I telescope to investigate AGN identification at multiple wavelengths and their host galaxy properties at $z \sim 1.37$–3.80. Considering data from the first season of the MOSDEF survey, Coil et al. (2015) found that while the BPT diagram works well for identifying optical AGNs at $z \sim 2$, it cannot provide a complete sample of AGNs, as it suffers from biases against low mass and/or high specific star formation rate (sSFR) host galaxies. In this paper, with a larger data set from the first two years of the MOSDEF survey, we identify optical AGNs using the BPT diagram and use additional AGN samples selected a priori based on X-ray and IR imaging data to investigate the selection biases from each identification method. We explore the host galaxy properties of these AGNs and investigate the relation between SF and AGN luminosity in our sample at the epoch of the peak of both AGN and galaxy growth.

The outline of the paper is as follows: in Section 2 we describe the X-ray and IR data used to identify AGNs in MOSDEF, along with the method used for measuring the optical emission line ratios that is used for identifying optical AGNs. In this section we also provide information about stellar mass and SFR estimates in our sample. In Section 3 we present our results on the AGN host galaxy properties and the relation between AGN activity and SFR at $z \sim 2$. In Section 4 we discuss our results, and we conclude in Section 5. Throughout the paper we adopt a flat cosmology with $\Omega_\Lambda = 0.7$ and $H_0 = 72 \, \mathrm{km \, s^{-1} \, Mpc^{-1}}$.

2. SAMPLE AND MEASUREMENTS

In this study, we use multi-wavelength data from the MOSDEF survey to investigate AGN host galaxy properties at $z \sim 2$. We use X-ray imaging data from *Chandra*, IR imaging data from *Spitzer-IRAC*, and rest-frame optical spectra obtained with the MOSFIRE spectrograph at Keck Observatory to identify AGNs. We describe these data sets below, as well as our methods for fitting the optical emission lines in our spectra and for estimating stellar masses and SFRs of AGN host galaxies by fitting their SEDs.

2.1. The MOSDEF Survey

In this study, we use spectroscopic data from the MOSDEF survey (Kriek et al. 2015). This survey uses the MOSFIRE spectrograph (McLean et al. 2012) on the 10 m Keck I telescope. MOSFIRE provides wavelength coverage from 0.97 to 2.40 μm with a spectral resolution of $R = 3400, 3300, 3650,$ and 3600 respectively in the Y, J, H, and K bands. MOSDEF observations cover a total area of 500 arcmin^2 in three extragalactic fields: COSMOS, GOODS-N, and EGS from the CANDELS survey (Grogin et al. 2011; Koekemoer et al. 2011) in areas with 3D-*Hubble Space Telescope* (*HST*) grism survey (Brammer et al. 2012) coverage. Along with *HST* imaging, there are extensive multi-wavelength ancillary data from other telescopes including *Chandra, Spitzer*, and *Herschel* for MOSDEF targets. In this paper we use data from the first two years of the survey. During this time observations were also taken in the GOODS-S and UDS fields, in addition to the main survey fields above, and these data are included here.

MOSDEF targets span a wide range of redshift from $1.37 < z < 3.80$ and when completed, the survey will include $\sim$1500 galaxies and AGNs. The targets are chosen from three distinct redshift intervals ($1.37 < z < 1.70$, $2.09 < z < 2.61$ and $2.95 < z < 3.80$) to ensure that the rest-frame optical emission lines fall within windows of atmospheric transmission. Sources in MOSDEF are targeted down to limiting *HST*/WFC3 F160W magnitudes of 24.0, 24.5, and 25.0, respectively, at $z \sim 1.5, 2.3$, and 3.4 using the 3D-*HST* photometric catalogs (Skelton et al. 2014). Target priorities in MOSDEF are determined by their brightness and redshift information, with brighter sources and those with more secure prior redshift determinations given higher weights. AGNs identified in advance via X-ray or IR imaging are also given higher targeting weights. In data from the first two years of the MOSDEF survey, which we use here, we identify 482 galaxies and 55 AGNs. Detailed information about the MOSDEF AGN sample is provided below. The full details of the survey, data reduction and analysis are presented in Kriek et al. (2015).

2.2. X-ray AGN Selection

The X-ray AGNs in our sample were identified prior to MOSDEF targeting using the *Chandra* imaging in our fields, which had a depth of 4 Ms in GOODS-S, 2 Ms in GOODS-N, 800 ks in EGS and 160 ks in COSMOS (at the time of MOSDEF target selection). We use catalogs generated in a consistent manner as described by Laird et al. (2009) and Nandra et al. (2015) (see also Georgakakis et al. 2014; Aird et al. 2015). Our adopted Poisson false probability detection threshold ($< 4 \times 10^{-6}$) corresponds to reaching hard band flux ($f_{2-10 \, \mathrm{keV}}$) limits (over $>10\%$ of the area) of 1.6×10^{-16}, 2.8×10^{-16}, 5.0×10^{-16} and 1.8×10^{-15} in the GOODS-S,

GOODS-N, EGS, and COSMOS fields, respectively (although we note that the depths of the *Chandra* imaging vary substantially within a field).

We use the likelihood ratio technique to identify reliable optical, NIR, and IRAC counterparts to the X-ray sources (as described in Aird et al. 2015; see also Sutherland & Saunders 1992; Ciliegi et al. 2003; Brusa et al. 2007; Laird et al. 2009). For sources with multiple counterparts, we choose the match with the highest likelihood ratio. Finally, we match our catalog of X-ray counterparts to the 3D-*HST* catalogs used for MOSDEF targeting and find the closest 3D-*HST* match within 1″.

For our X-ray AGNs, we estimate the rest-frame 2–10 keV X-ray luminosities based on the hard (2–7 keV) observed flux or, if the source is not detected in the hard band, the soft (0.5–2 keV) observed flux. We assume a simple power-law spectrum including only Galactic absorption with a photon index of $\Gamma = 1.9$. We do not correct our X-ray luminosities for intrinsic absorption effects (local to the AGN). At $z \sim 2.3$, only about 10% of the observed X-ray flux is suppressed at a column density of $10^{23}\,\mathrm{cm}^{-2}$. Therefore, our estimates of the X-ray luminosity are accurate and larger absorption column densities ($N_{\mathrm{H}} > 10^{23}\,\mathrm{cm}^{-2}$) are required to significantly suppress the observed flux at $z \sim 2$.

In total, there are 28 X-ray AGNs in the current MOSDEF sample, 22 of which are detected in the hard band with X-ray luminosities ($L_{\mathrm{X}(2-10\,\mathrm{keV})}$) within the range of 10^{43}–10^{45} erg s^{-1}. Given the relatively high X-ray luminosities of these sources, we do not impose any luminosity cut on the X-ray AGN sample.

2.3. IR AGN Selection

Using hard X-ray (2–10 keV) detections ensures that our sample is not strongly biased against moderately obscured ($N_{\mathrm{H}} \sim 10^{22-24}\,\mathrm{cm}^{-2}$) AGNs; however, hard X-ray radiation cannot penetrate Compton-thick regions with heavy obscuration ($N_{\mathrm{H}} > 10^{24}\,\mathrm{cm}^{-2}$). In heavily obscured AGNs, the high-energy nuclear emission is absorbed and reprocessed by dust near the AGN and re-radiated at MIR wavelengths. This re-radiated emission from dust results in MIR imaging also being useful in identifying AGNs.

Several MIR AGN selection techniques have been proposed using data from the IRAC (Fazio et al. 2004) on *Spitzer* (e.g., Lacy et al. 2004; Stern et al. 2005; Alonso-Herrero et al. 2006; Donley et al. 2008, 2012). Depending on the depth of the data and the redshift of interest, some of these criteria can suffer from contamination from star-forming galaxies mis-identified as AGNs. In starburst galaxies or galaxies with older stellar populations and/or higher dust extinction the stellar bump can mimic the power-law emission from AGNs.

The Stern et al. (2005) criteria, which were empirically derived from shallow, wide-area *Spitzer* data, have been shown to be unreliable at various redshifts ($z \sim 1$ and $z \gtrsim 2.5$) (e.g., Georgantopoulos et al. 2008; Donley et al. 2012; Mendez et al. 2013). Here, using IRAC fluxes from v4.1 of the 3D-*HST* catalogs (Skelton et al. 2014), after removing X-ray AGNs, we find that ~10% of the full MOSDEF sample falls within the Stern et al. (2005) selection region (only ~38% of these sources are IR AGNs using the Donley et al. 2012 criteria), indicating that the Stern et al. (2005) selection may be contaminated by star-forming galaxies at the redshift and depth of our survey.
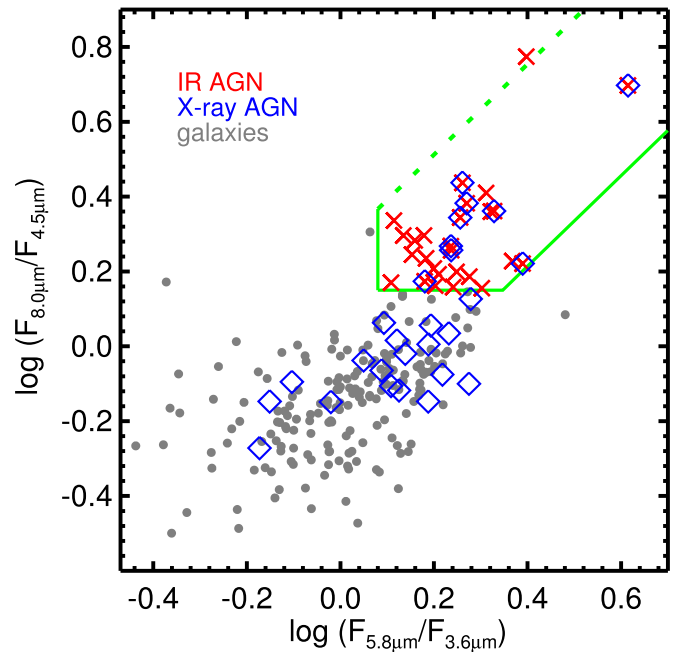

Figure 1. IRAC color–color space for MOSDEF sources, where criteria from Donley et al. (2012) defined in Equations (2)–(4) in the text are shown in green. The gray points show MOSDEF galaxies, and the blue diamonds are X-ray AGNs identified in Section 2.2. The red points show the sources that fall inside the Donley-defined wedge and therefore are selected as IR AGNs.

Donley et al. (2012) provide more reliable IR AGN identification criteria, which are designed to limit the contamination from star-forming galaxies, especially at high redshift. The robustness of this selection technique in identifying IR AGNs from star-forming galaxies is confirmed by Mendez et al. (2013), using a large faint galaxy sample at intermediate redshifts. In the Donley et al. (2012) selection criteria, objects are required to be detected in all four IRAC bands and satisfy the following criteria in IRAC color–color space:

$$x = \log_{10}\left(\frac{f_{5.8\,\mu\mathrm{m}}}{f_{3.6\,\mu\mathrm{m}}}\right),\ y = \log_{10}\left(\frac{f_{8.0\,\mu\mathrm{m}}}{f_{4.5\,\mu\mathrm{m}}}\right) \tag{1}$$

$$x \geqslant 0.08 \text{ and } y \geqslant 0.15 \text{ and} \tag{2}$$

$$y \geqslant (1.21 \times x) - 0.27 \text{ and} \tag{3}$$

$$y \leqslant (1.21 \times x) + 0.27 \text{ and} \tag{4}$$

$$f_{4.5\,\mu\mathrm{m}} > f_{3.6\,\mu\mathrm{m}} \text{ and} \tag{5}$$

$$f_{5.8\,\mu\mathrm{m}} > f_{4.5\,\mu\mathrm{m}} \text{ and} \tag{6}$$

$$f_{8.0\,\mu\mathrm{m}} > f_{5.8\,\mu\mathrm{m}} \tag{7}$$

In MOSDEF we identify IR AGNs using these criteria, with some slight modifications. In addition to the detection in all four IRAC bands, we set a flux limit in each band that corresponds to a signal-to-noise ratio (S/N) respectively in channels 1 to 4 of 3, 3, 2.4, and 2.1 (see Mendez et al. 2013 for an explanation of how these limits are derived).

Figure 1 shows the relevant IRAC color–color space of $\log(f_{8.0\,\mu\mathrm{m}}/f_{4.5\,\mu\mathrm{m}})$ versus $\log(f_{5.8\,\mu\mathrm{m}}/f_{3.6\,\mu\mathrm{m}})$. The green solid and dashed lines indicate the criteria defined in Equations (2)–(4), and enclose an area referred to as the "Donley wedge." The gray points are galaxies in the MOSDEF sample and the blue diamonds are X-ray AGNs identified in Section 2.2. The red

points show the sources that fall inside the Donley wedge and therefore are selected as IR AGNs. There is one red source above the dashed line that satisfies all the above criteria except for Equation (4). The IRAC photometry for this source indicates a sharp increase in the flux from channel 1 to 4, which is common only in IR AGNs. Since none of the galaxies in MOSDEF lie close to the dashed line, we relax the upper bound on Donley wedge, showing it with a dashed line in Figure 1 and including this red source in our IR AGN sample. There are also three sources inside the Donley wedge that satisfy all the above criteria except for one of the Equations (5), (6) or (7), which require a strictly increasing, red power-law SED in the IRAC bands. We relax these three criteria such that any source consistent with an increasing red power-law *within the 1σ errors on the IRAC photometry* is classified as an IR AGN. We note that 32% of the X-ray AGNs lie inside the Donley wedge, which indicates that they are identified as AGNs based on both the X-ray and IRAC imaging data. In total we identify 27 IR AGNs in the current MOSDEF sample, 9 of which are also detected in X-rays.

2.4. Spectroscopic Data and Optical AGN Selection

The MOSDEF survey has obtained spectroscopic data using the MOSFIRE spectrograph, which enables us to detect emission lines at rest wavelengths of 3700–7000 Å for our sources. These data enable us to use optical diagnostics such as the BPT diagram (Baldwin et al. 1981; Veilleux & Osterbrock 1987) to identify AGNs that may not be detectable with X-ray or IR imaging data. In this section we describe the emission line fitting procedure we used for measuring the flux of each line, and the AGNs that are identified with optical diagnostics.

2.4.1. Optical Emission Line Flux Measurements

In order to use optical diagnostics to identify AGNs in our sample, we need to measure the Hβ, [O III], Hα, and [N II] emission lines. We fit Gaussian functions to the observed lines using the MPFIT nonlinear least-squares fitting function in IDL (Markwardt 2009), using the error spectra to determine the errors on the fit. We simultaneously fit [O III] $\lambda 5008$ with [O III] $\lambda 4960$, and Hα with [N II] $\lambda 6550$ and [N II] $\lambda 6585$. We fix the continuum to be flat, with no slope, and allow up to 0.15% freedom to the centroid of the expected narrow and broad lines wavelength. We require the same physical component (i.e., narrow line, broad line) to have the same FWHM and velocity offset in each line, as determined from the line with the highest S/N. We fix the spacing between the [O III] $\lambda 4960$ and [O III] $\lambda 5008$ forbidden lines and fix their relative normalizations to a ratio of 1:3 (as well as for the [N II] $\lambda 6550$ and [N II] $\lambda 6585$ lines). For each source we consider four different models for the emission line profiles, with various components, as described below.

In model 1, we fit each line with a single Gaussian function with the same centroid velocity and FWHM which is required to be $< 2000\,\mathrm{km\,s^{-1}}$, representing the narrow emission line component. In model 2, we fit each line with a narrow Gaussian component and additionally for Hβ and Hα include a broad Gaussian component (FWHM $> 2000\,\mathrm{km\,s^{-1}}$) representing emission from the AGN broad-line region. In model 3, we fit each line with two Gaussian components, one narrow line component as above and a second component with a FWHM $< 2000\,\mathrm{km\,s^{-1}}$ and a negative velocity offset
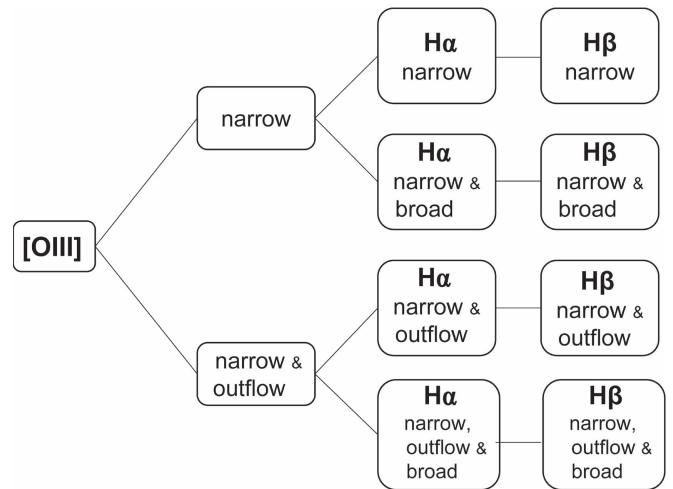

Figure 2. A flowchart representing the logic of our Gaussian emission line fitting procedure. In each step we evaluate any change in χ^2 to establish whether the additional components results in an improved fit (at the 99% confidence level). We first evaluate the fit to [O III] to determine whether an additional outflow component is required. We then evaluate whether the Hα fit requires a broad component (also including an outflow component if required by [O III]). Lastly, we fit Hβ with the same components as Hα.

$(-500 < v < 0\,\mathrm{km\,s^{-1}})$ relative to the narrow line component, representing an outflow that could be driven by an AGN (G. C. K. Leung et al. 2016 in preparation). The FWHM and centroid velocity of the outflow component is fixed to be identical for all of the emission lines. In model 4, we fit each line with narrow and outflow components, and additionally allow for a broad component with an identical FWHM ($> 2000\,\mathrm{km\,s^{-1}}$) to the Hβ and Hα lines.

In each model we evaluate any change in reduced χ^2 to establish whether the additional components result in an improved fit at confidence level of 99%. Figure 2 is a flowchart that shows the order of our fitting procedure. We first evaluate the reduced χ^2 from model 1 to model 3 for the [O III] line to see if the additional outflow component has improved the fit. If so, we then evaluate the Hα fit from model 3 to 4 to see if an additional broad component improves the fit. If the [O III] line is well fit with only a narrow component, we then compare the Hα fit in model 1 with model 2 to see whether the additional broad component improves the fit.

To find the minimum width of the Gaussian components, we identify sky lines in each wavelength filter for each source, fit them with a single Gaussian component, and use their average width as the minimum width of the narrow line fits. This sets the minimum width for the velocity dispersion of 2.5 Å in the observed H band and 3.5 Å in the observed K band, which at $z \sim 2.3$ corresponds to $\sim 45\,\mathrm{km\,s^{-1}}$ and $\sim 48\,\mathrm{km\,s^{-1}}$ respectively in H and K bands. The minimum width for the broad Gaussian component is set by the upper limit on the FWHM ($< 2000\,\mathrm{km\,s^{-1}}$) of the narrow lines.

Figure 3 illustrates examples of MOSDEF spectra for four different AGNs in our sample, with the best-fit result of our multiple-component fitting procedure. The overall fit is shown in blue, and the individual components are shown in different colors. The top panel shows an AGN where a narrow Gaussian component is the best fit to all the lines. The second panel shows an AGN with a narrow component for all lines and an additional broad component to Hβ and Hα. The third panel
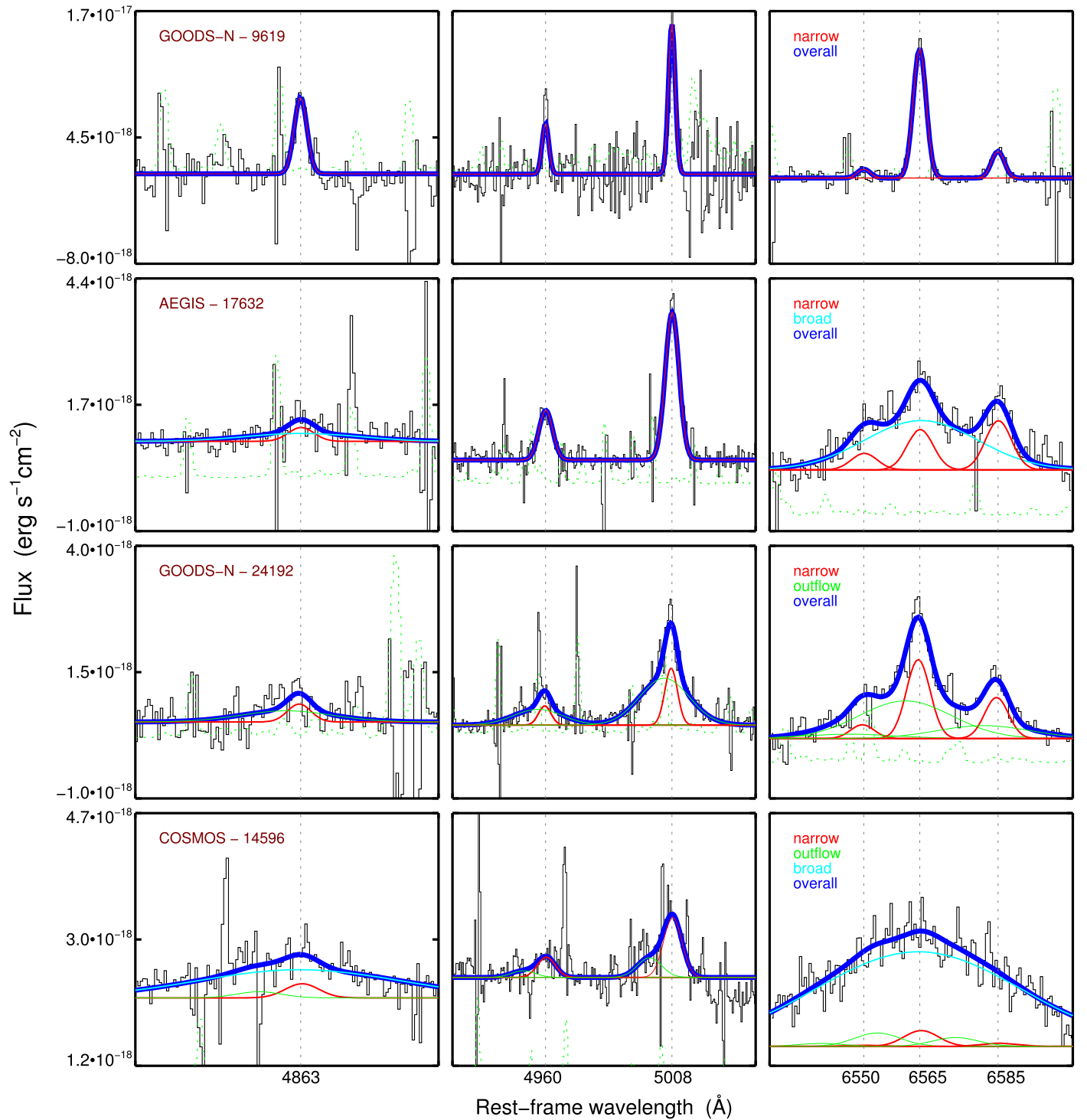
Figure 3. Examples of MOSDEF spectra and the multiple-component fitting procedure for four AGNs in our sample (the IDs are from v4.1 of the 3D-*HST* catalogs). The overall fit is shown in blue, while the individual Gaussian components are shown in different colors: red for the narrow component, green for an outflow, and cyan for a broad component. The error spectra are shown with dotted green lines, while vertical dotted gray lines show the rest frame wavelength of the emission lines we fit. The top row shows an AGN where only a narrow Gaussian component is required to all of the lines. The second row shows an AGN that requires an additional broad component to Hβ and Hα . The third row shows an AGN with a clear outflow component, detected in the [O III] and Hα lines. The fourth row shows an AGN that requires both an outflow component (seen in [O III] λ5008) and a broad component. Sources that have a broad Hα and/or Hβ component with the S/N $>$ 3 are excluded from our analysis in Section 3, as we cannot reliably probe their host galaxy properties.

shows an AGN with a significant outflow component for both the [O III] and Hα lines, in addition to the narrow component. In the last panel in addition to the outflow component (seen in the [O III] λ5008 line), the Hα fit improves with an underlying broad component.

In our spectral fits, we find that four AGNs (identified at both X-ray and IR wavelengths) require a broad Hα and/or Hβ component with the S/N $>$ 3. Since we cannot reliably probe the host galaxy properties of these AGNs, we exclude them for the analysis in Section 3. We keep these sources in our
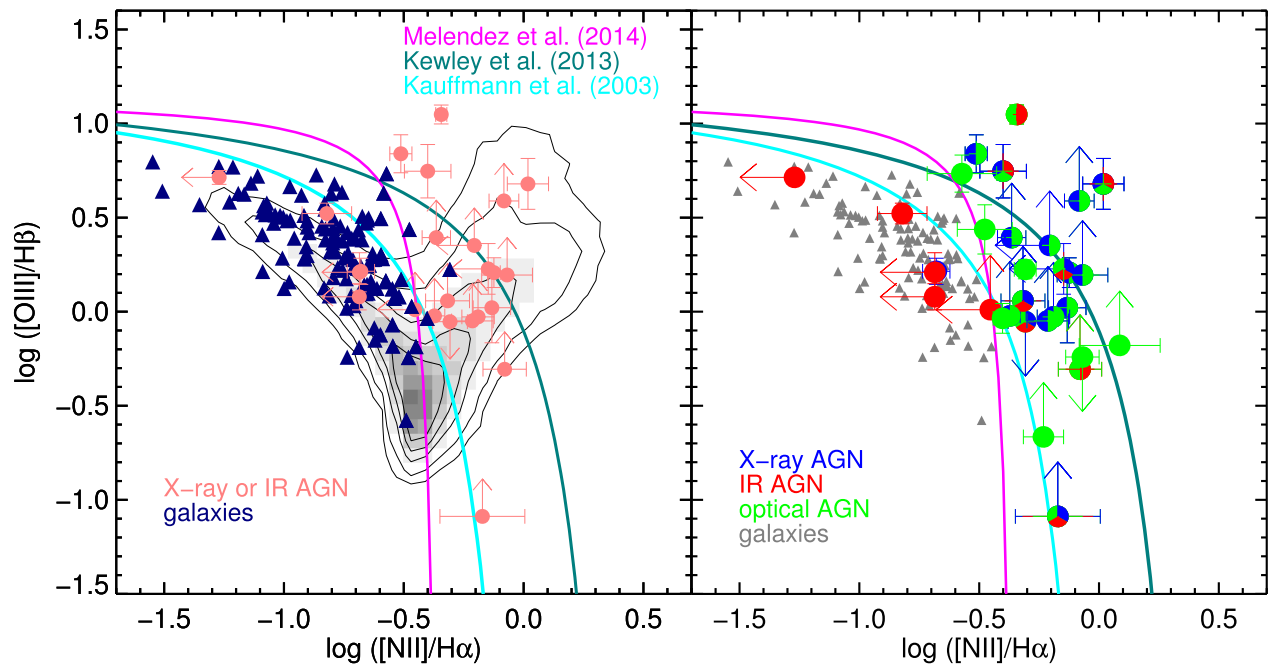
Figure 4. The BPT diagram for MOSDEF AGNs and galaxies. Left: Pink circles show AGNs identified with X-ray and/or IR imaging, with arrows showing 3σ limits for AGNs for which all four relevant optical emission lines are not detected in MOSDEF. Dark blue triangles show MOSDEF galaxies (with $>3\sigma$ detections of all four relevant optical emission lines). The contours and grayscale show the location of SDSS sources in this plane. The cyan line is the empirical criteria from Kauffmann et al. (2003) that indicates the division between star-forming galaxies and AGNs in SDSS. The dark green line is the theoretical prediction from Kewley et al. (2013) of the maximum line ratios expected for starburst galaxies, in the absence of an AGN. The magenta line is the theoretical prediction for identifying AGNs by Meléndez et al. (2014). Here we use this line to identify optical AGNs in MOSDEF, as this line most cleanly separates known X-ray and/or IR AGNs from galaxies in our sample. Right: Similar to the left panel but here MOSDEF AGNs are shown using different colors that indicate the wavelength used to identify them as AGNs. X-ray AGNs are shown in blue, IR AGNs are shown in red, and optical AGNs (identified as lying above the Meléndez et al. 2014 line) are shown in green. The AGNs that are identified using more than one wavelength method are shown with multiple colors. The MOSDEF galaxies with $>3\sigma$ detections of all four of the necessary emission lines are shown in gray.

sample for the purpose of identifying optical AGNs below in Section 2.4.2, but we do not consider the contributions from the broad optical emission lines.

We note that for all sources where the best fit included an outflow component, we visually inspected the *HST* imaging to determine whether they might be merger candidates; in these cases the "outflow" component might not be from an outflow, but from a merger event. We identified six sources (ID = 28202, 26028, 22299, 16339, 9183, 3146 in v4.1 of 3D-*HST*) with two potential nuclei that indicate that the host galaxies of these AGNs may be undergoing merger events. Since it is not clear which of the two components has the detected AGN, and since the photometry of the two components will often be blended for these sources, we exclude them from the analysis of AGN spectral or host galaxy properties in this paper. Of the 28 X-ray AGNs in our sample, four are merger candidates, while from the 27 IR AGNs, 2 are merger candidates.

2.4.2. Optical AGN Sample

We use the fluxes from our line fitting procedure to measure the [N II]/Hα and [O III]/Hβ line ratios, required to place sources on the BPT diagram. We do not include broad components in these fluxes. We correct the flux of the narrow components of the Hβ and Hα lines for underlying stellar absorption, using the best-fit SED models to the multi-wavelength photometry (for more details see Reddy et al. 2015). This correction results in an average change of $\sim$0.01 and $\sim$0.06 dex respectively in log([N II]/Hα) and log([O III]/

Hβ) line ratios on the BPT diagram and thus has a small effect on our sample.

Figure 4 shows the BPT diagram for MOSDEF AGNs and galaxies. In the left panel, AGNs identified at either X-ray or IR wavelengths are shown with pink circles; the remaining MOSDEF sources (with $>3\sigma$ detections of all four of the necessary emission lines) are shown with blue triangles. We note that there are galaxies with $<3\sigma$ detections that are not shown in this panel. For the X-ray and IR selected AGNs, since they are already identified as AGNs with reliable methods we require a significant ($>3\sigma$) detection of at least one of the two lines required for each ratio. If the other line is not significantly detected, we use the 3σ limit on the flux to determine the limit on the line ratio (indicated by the arrows in Figure 4). For the 40 X-ray and/or IR detected AGNs in our sample, we are able to place 24 AGNs on the BPT diagram (including those with limits).

For comparison, we show the location of SDSS sources with contours and grayscale in this panel. The cyan line is the empirical demarcation from Kauffmann et al. (2003) that shows the division between star-forming galaxies and AGNs in the SDSS. The dark cyan line is the theoretical prediction from Kewley et al. (2013) of the maximum line ratios expected in starburst galaxies, in the absence of an AGN. We also show in magenta the theoretical prediction for the lowest line ratios allowed by AGNs of Meléndez et al. (2014).

Sources that lie between the Kauffmann et al. and Kewley et al. lines are often referred as "composite" sources, in that their line ratios can have contributions from both SF and AGN activity. For sources to the right of the Kewley et al. (2013)
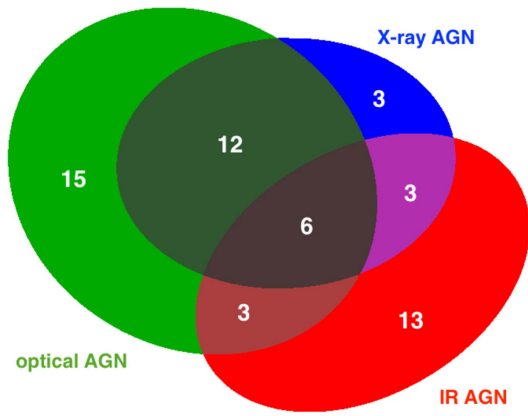
Figure 5. A Venn diagram showing the number of AGNs in our sample identified at different wavelengths; the full sample contains 55 AGNs (and 482 galaxies). The overlapping regions show the number of AGNs selected at multiple wavelengths. This diagram shows our detected AGN sample and is not corrected for observational biases such as the depth of the data at each wavelength.

line, such high line ratios can only be due to AGN activity (e.g., Shapley et al. 2015). We note that the galaxies in our sample lie above the main locus of star-forming galaxies in the SDSS in $\log([\text{O III}]/\text{H}\beta)$ and/or $\log([\text{N II}]/\text{H}\alpha)$ (by a median offset of $\sim$0.1 dex, see Coil et al. 2015; Shapley et al. 2015). This offset has been seen in other studies of high-redshift galaxies (e.g., Yabe et al. 2012; Masters et al. 2014; Newman et al. 2014; Steidel et al. 2014). Applying a luminosity limit to the SDSS sample that is comparable to the limit for high-redshift galaxies reduces this offset somewhat (Juneau et al. 2014) but as shown in Coil et al. (2015) the offset does not completely disappear.

Figure 4 shows that the Kauffmann et al. (2003) line may not be as reliable as a means of separating galaxy and AGN populations at $z \sim 2$ as at $z \sim 0$. On the other hand, using the Kewley et al. (2013) line, which demarcates a pure sample of AGNs, results in a highly incomplete and restricted AGN sample. In fact, the majority of the X-ray or IR detected AGNs in the MOSDEF sample lie below the Kewley et al. (2013) line. As discussed in Coil et al. (2015), the Meléndez et al. (2014) line can be used to more reliably separate galaxies and AGNs in MOSDEF. The left panel of Figure 4 shows that the vast majority of the X-ray and IR detected AGNs in our sample lie above this line, while the majority of the other MOSDEF sources lie below this line. Therefore in this study we identify all sources with line ratios that are above this line as optical AGNs.

The right panel of Figure 4 shows the BPT diagram for MOSDEF sources, using the above classification of AGNs at different wavelengths. For AGNs that are identified using multiple wavelengths, we use multiple colors based on their identification methods. MOSDEF galaxies with at least 3σ detections in all four lines are shown with gray triangles. We emphasize that in addition to the four sources above the Meléndez et al. (2014) line in the left panel of Figure 4 which we identify as optical-only AGNs, there are 11 sources with 3σ detections in both Hα and [N II] λ6585 without reliable Hβ and [O III] λ5008 detections. We also classify these sources as optical AGNs due to their high $\log([\text{N II}]/\text{H}\alpha)$, which is greater than -0.3.

Using a UV-selected galaxy sample, Steidel et al. (2014) find a larger offset for star-forming galaxies in the BPT diagram,
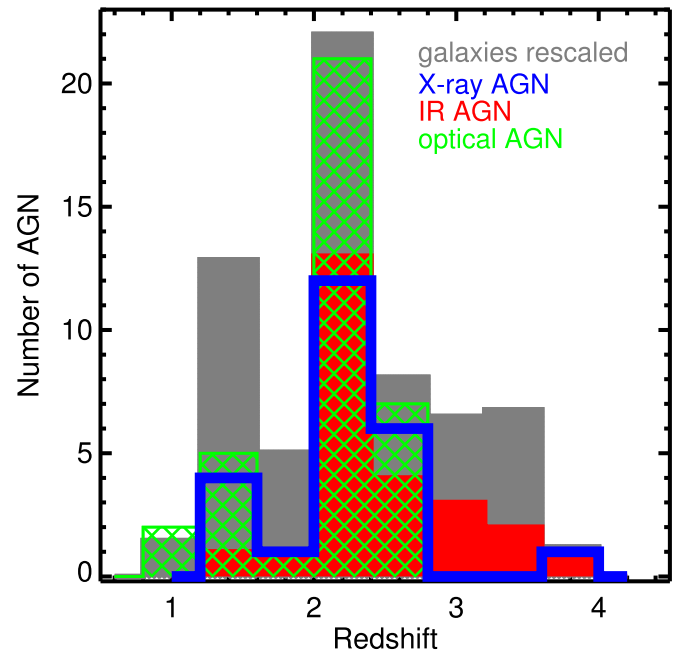

Figure 6. The redshift distribution for the 55 AGNs and 482 galaxies in the MOSDEF sample. The distribution for each identification technique is shown with a different color. AGNs identified at multiple wavelengths are counted in each distribution and can therefore be represented multiple times in this figure.

compared with local samples. Using the Meléndez et al. (2014) line to identify optical AGNs in their sample would lead to a larger AGN fraction than in the MOSDEF sample and may lead to more contamination by star-forming galaxies in their sample. Instead, a more strict criterion of $\log([\text{N II}]/\text{H}\alpha) > -0.3$ could be used. In the MOSDEF sample, however, using this cut results in only four sources being removed from the optical AGN sample and therefore does not change any of our conclusions. Since the Meléndez et al. (2014) line provides the cleanest separation between known AGNs and galaxies in the MOSDEF sample, we use it here. We also note that it is unlikely that the integrated light of many of our sources to be dominated by shocks, which could potentially also move sources above the Meléndez et al. (2014) line.

For the sample used here, there are 40 X-ray and/or IR AGNs, of which 21 are also identified as optical AGNs. In addition, there are 15 sources classified as optical AGNs that are only identified as AGNs through optical diagnostics. In total, there are 55 AGNs in the MOSDEF sample. Figure 5 is a Venn diagram illustrating the number of AGNs identified at different wavelengths in our sample. We use ellipses instead of circles in the Venn diagram, so that the areas are proportional to the number of AGNs identified with each method.

Figure 6 illustrates the redshift distribution for AGNs and galaxies in our sample. Each color represents the redshift distribution for a different identification technique, and as a single AGN can be detected at multiple wavelengths it can contribute to more than one histogram in this figure. While our AGNs span a wide range of redshifts, they strongly peak at $z \sim 2$, due to the MOSDEF target selection. We note that we cannot identify optical AGNs at $z > 2.6$, as at these redshifts the Hα and [N II] λ6585 lines fall beyond the observed wavelength coverage of our MOSFIRE spectra.

2.5. Stellar Mass and SFR Estimates

To measure the SFR and stellar mass of the AGN host galaxies, we use SED fitting, which is a widely adopted method for estimating physical properties of galaxies. We use the FAST stellar population fitting code (Kriek et al. 2009) with the multi-wavelength photometry from 3D-*HST* (Skelton et al. 2014) and the MOSDEF spectroscopic redshifts. We adopt the Conroy et al. (2009) Flexible Stellar Population Synthesis models, along with a Chabrier (2003) stellar initial mass function (IMF), the Calzetti et al. (2000) dust reddening curve and use a fixed solar metallicity. We consider delayed exponentially declining SF histories, $\Psi \propto t \exp(\frac{-t}{\tau})$, where t is the time since the onset of SF and τ is the characteristic SF timescale and is within the range of $0.1 < \tau < 10$ Gyr. FAST searches over a grid of models and uses χ^2 fitting to determine the best-fit solution (Kriek et al. 2009).

There is one AGN (identified at both X-ray and optical wavelengths) in our sample that is not fully spatially covered by the CANDELS imaging in the COSMOS field, such that the photometry is underestimated at the CANDELS wavelengths; therefore we do not include this AGN when presenting results from SED fits in this paper.

Light from the AGN may contribute to the observed SED, particularly at UV and IR wavelengths, which can impact our estimates of the SFR and stellar mass of the host galaxy. The Wien tail of the blackbody radiation from dust grains near the SMBH can be fit with a red power-law at MIR wavelengths. Therefore, to take into account any possible contribution from the AGN, we subtract power-laws with varying slopes and normalizations in both the UV and MIR from the observed photometry and re-run FAST on the remaining flux. We then choose the fit with the lowest reduced χ^2 as the best fit across all of the possible inputs (including no power-law subtraction, i.e., all galaxy light).

To create the grid of power-law SEDs to subtract, for both UV and MIR wavelengths, we allow the normalization to vary from 0% to 100% in terms of the observed flux in the U and IRAC channel 3 (5.8 μm) bands. We assume power-laws of the form $F_\nu \propto \nu^\alpha$, where we allow α to range from 0 to 0.5 for the UV and -5 to -0.5 in the MIR. We note that Ivezić et al. (2002) considered a wider range of the optical spectral indices, $-2 \leqslant \alpha \leqslant 0.5$, based on the quasars in SDSS sample, but we consider a more limited range as the AGNs in our sample are all lower luminosity and are type 2 AGNs that are not expected to be dominated by the AGN component in the optical. We subtract the blue power-law from the photometry at rest-frame wavelengths <1 μm.

For subtracting the red power-law corresponding to the AGN contribution at MIR wavelengths, we initially considered slopes within the range of -3 to -0.5, following Donley et al. (2012). However, we found that a redder slope was often needed to describe the observed slope of the SED for the two reddest IRAC channels (3 and 4) and thus adjusted our limits to allow for slopes as red as $\alpha_{\rm IR} > -5$. We subtract the IR power-laws from the photometry at rest-frame wavelengths >1 μm to avoid any unnecessary subtraction from other bands. The power-law subtraction allows us to correct for any possible contamination from AGNs in our SED-derived host galaxy properties.

Figure 7 shows two examples of the original 3D-*HST* photometry and the power-law subtracted photometry for an AGN identified at both X-ray and IR wavelengths (top panel)
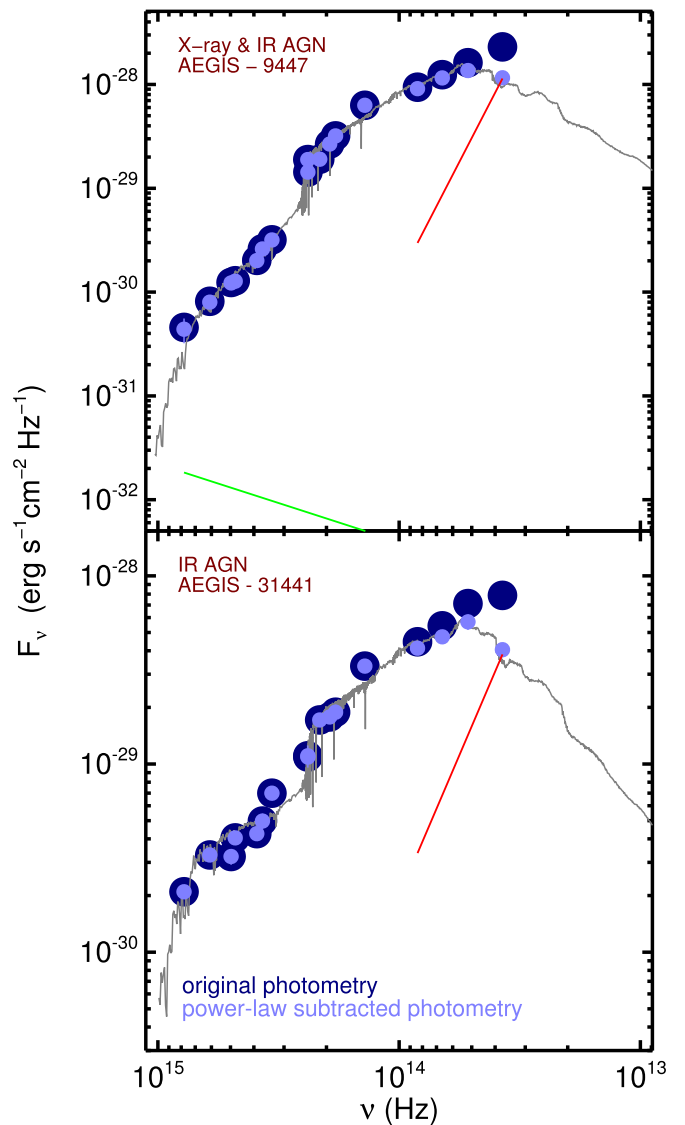

Figure 7. The observed photometry (dark blue) and power-law subtracted photometry (light blue) for two AGNs in the MOSDEF sample. The green line shows the power-law subtracted from the original photometry at rest-frame wavelengths <1 μm, and the red line shows the power-law subtracted from the original photometry at rest-frame wavelengths >1 μm. The top panel shows an X-ray and IR AGN, where subtracting a blue power-law at UV and optical wavelengths and a red power-law at MIR wavelength results is a reduced χ^2 smaller than the fit to the original photometry. The bottom panel shows an IR AGN where the best fit requires subtracting only a red power-law, as shown.

and an IR-only AGN (bottom panel). The green line shows the power-law subtracted from the original photometry at rest-frame wavelengths <1 μm, while the red line shows the power-law subtracted from the original photometry at rest-frame wavelengths >1 μm. In the top panel, subtracting the blue power-law at UV and optical wavelengths and the red power-law at MIR wavelengths results in a better fit. For the IR AGN in the bottom panel, subtracting only a red power-law at MIR wavelengths results in a better fit.

Using this method leads to a more robust estimate of SFR and stellar mass for AGN host galaxies. Santini et al. (2012) find that, for type 2 AGNs, stellar mass estimates derived from pure stellar templates are within a factor of two of the estimates derived including both stellar and AGN templates (with a mean difference of zero). Subtracting the AGN contribution from the

original photometry as we do here leads to a 0.13 dex decrease in the average SFR and an 0.03 dex (in logarithmic space) decrease in the average stellar mass of the AGNs in our sample.

Here we run the FAST code without using the so-called template error function, which can be used to account for any wavelength-dependent mismatch between the observed photometry of sources and the templates used (Brammer et al. 2008; Kriek et al. 2009, 2015). We find that the SFRs and stellar masses estimated from FAST without the template error function after subtracting power-laws are consistent with those derived from the original photometry using the template error function; this indicates our method for estimating SFR and stellar mass is robust.

2.6. [O III] Luminosity as a Proxy of AGN Activity

The [O III] emission line traces photoionized gas clouds in the narrow line region of AGNs and is a good proxy for measuring nuclear activity (e.g., Kauffmann et al. 2003; Heckman et al. 2005). However, SF activity can also produce a narrow [O III] emission line, which can contaminate the signal from the AGN. At low redshifts, studies have used different methods to attempt to disentangle AGN and SF contributions to the [O III] emission line (e.g., Kauffmann & Heckman 2009; Wild et al. 2010; Tanaka 2012). In this section we investigate whether these methods are applicable to higher-redshift samples and estimate the contribution from SF to [O III] luminosity in our sample.

Kauffmann & Heckman (2009) and Wild et al. (2010) use empirical techniques to estimate the contribution of SF to $L_{[O\ III]}$ by measuring the distance of each source in the BPT diagram from the main locus of SF. Kauffmann & Heckman (2009) find that the contribution to $L_{[O\ III]}$ from SF varies from $\sim$50% for sources on the Kauffmann et al. line to $\sim$10% for sources above the Kewley et al. line.

Alternatively, Tanaka (2012) use SED fitting to estimate the SFR for SDSS sources, and then convert this to an Hα luminosity using the Kennicutt (1998) relation, with an additional power-law as an extinction factor estimated at the Hα wavelength. They then fit a relationship to the observed ratio of [O III]/Hα with stellar mass and estimate $L_{[O\ III]}$ from SF for individual sources.

However, in our sample at $z \sim 2$, estimating the SF contribution to [O III] is more challenging, as we do not always have high S/N spectroscopic measurements of all of the relevant emission lines for all of our AGNs. Initially, we investigated the level of SF contamination for AGNs in the BPT diagram, using the method of Kauffmann & Heckman (2009). Out of the 55 AGNs in our sample, 31 have sufficient S/N to place them in the BPT diagram, though one of the two line ratios may be a limit. For these sources, we measure the distance of each AGN from the Kauffmann et al. line. However, we first shift the Kauffmann et al. line $\sim$0.1 dex higher in log([O III]/Hβ) to account for the overall offset of the MOSDEF galaxy sample compared to SF galaxies in the SDSS (see Figure 4 and Section 2.4.2 above); though we note that this shift could be along log([N II]/Hα) as well (see Shapley et al. 2015; Sanders et al. 2016). Figure 8 shows the histogram of the distance of each AGN on the BPT diagram in our sample from this modified Kauffmann et al. line.

For the AGNs that we can show on the BPT diagram, we find a median distance of 0.17 dex from the modified Kauffmann et al. line. This median point (log([N II]/
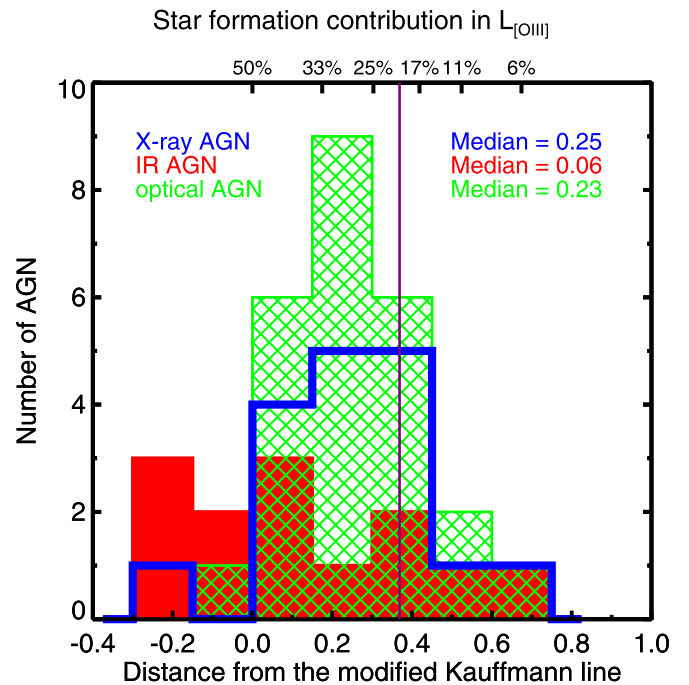

Figure 8. Histograms of the distance (in both [N II]/Hα and [O III]/Hβ) of each AGN population in the BPT diagram from the modified version of Kauffmann et al. (2003) line (see text for details). The top x axis indicates the fractional SF contribution to $L_{[O\ III]}$, according to Kauffmann & Heckman (2009). The median distance of our AGN sample is 0.17 dex which corresponds to a fractional contamination of $\sim$33%. The purple line roughly shows the distance of the Kewley et al. (2013) line, above which the contamination is less than 20%.

Hα) $= -0.39$, log([O III]/Hβ) $= 0.36$) lies in the Seyfert region of the BPT diagram, so we use the relevant trajectory from Kauffmann & Heckman (2009) to find the contribution of SF to the [O III] emission. The top x axis in Figure 8 shows the fractional SF contribution to $L_{[O\ III]}$. The median contribution for our AGNs is $\sim$33%. The purple line in Figure 8 roughly shows the distance of the Kewley et al. (2013) line. This indicates that AGNs above the Kewley et al. (2013) line should have a fractional SF contamination of less than 20%.

We also estimate the median SF contamination to $L_{[O\ III]}$ using the method of Tanaka (2012), as described above and find a median contamination of 30%. However, using this method we find a prohibitively large scatter which unfortunately indicates that we cannot use this method to apply a correction for SF on a source-by-source basis.

Here, we use $L_{[O\ III]}$ as a proxy of AGN activity as the majority of the [O III] flux is from the AGN (both methods described above estimate a $\sim$32% contribution from SF activity). Additionally, almost all of the AGNs in our sample lie in the AGN region of the BPT diagram (for optical AGNs this is by definition), which indicates their emission lines are dominated by AGN radiation rather than SF. We do not correct $L_{[O\ III]}$ for SF contamination here, as we cannot apply the Kauffmann & Heckman (2009) method since it requires reliable detections for each emission line, and using the Tanaka (2012) method results in a substantial additional scatter. As we discuss below in Section 3, any trends that we find with $L_{[O\ III]}$ are also confirmed with L_X in our X-ray detected sample, such that none of our results should be substantially impacted by SF contamination to [O III] .
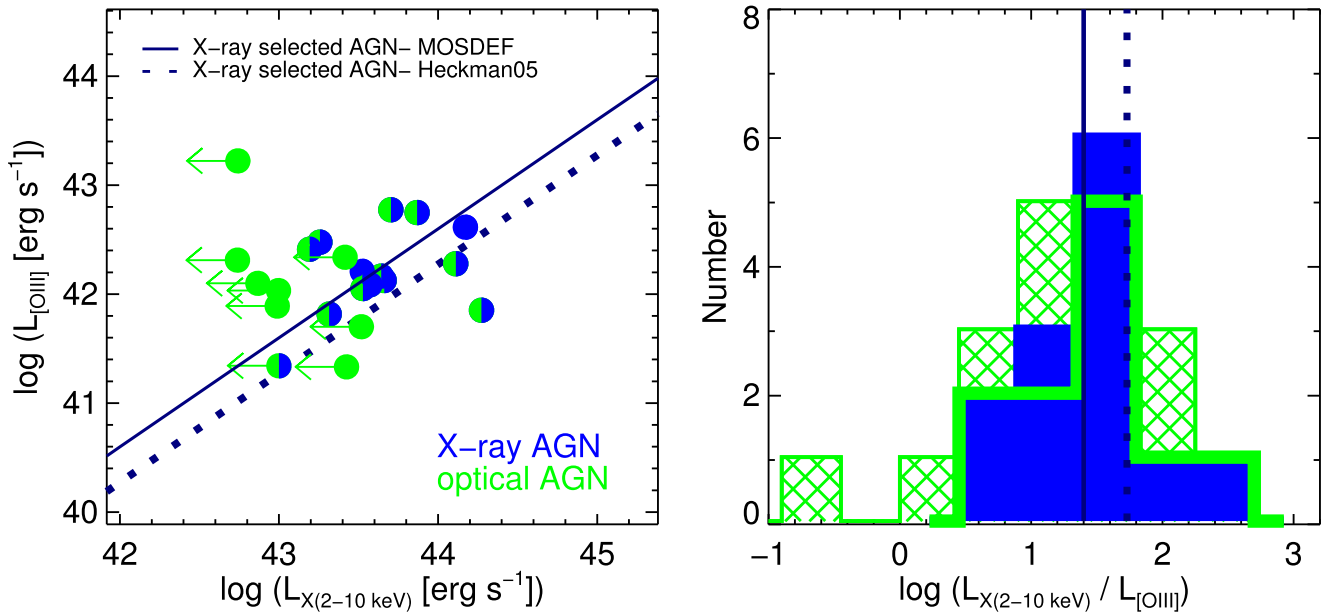
Figure 9. Left: $L_{[O\,III]}$ vs. $L_{X(2-10\,keV)}$ for X-ray (blue) and optical (green) AGNs. The arrows shows an upper limit on $L_{X(2-10\,keV)}$ for sources without X-ray detection. The solid light blue line shows the average $\log(L_X/L_{[O\,III]})$ (1.40 dex, with 0.44 dex standard deviation) for X-ray AGNs in MOSDEF while the dotted blue line shows the ratio (1.73 dex, with 0.41 dex standard deviation) for a sample of X-ray selected AGNs in Heckman et al. (2005). Right: The distribution of $\log(L_X/L_{[O\,III]})$ for X-ray AGNs and optically selected AGNs in MOSDEF. The solid green histogram indicates $\log(L_X/L_{[O\,III]})$ for the optically selected AGNs with X-ray identification, and the hashed histogram includes X-ray limits as well.

3. RESULTS

In this section we consider AGN identification at different wavelengths and investigate AGN selection biases and host galaxy properties for different identification techniques. We first compare the luminosities of AGNs selected at X-ray versus optical wavelengths. We then compare AGN host galaxy properties, such as SFR, dust content and stellar age, to a sample of inactive galaxies with the same distribution of stellar mass as the AGN host galaxies. Finally, we investigate the relationship between AGN activity and SFR in individual AGN host galaxies at $z \sim 2$. We emphasize that for any analysis with [O III] measurements we restrict our sample to sources with $>3\sigma$ [O III] $\lambda 5008$ detections, which includes 34 AGNs and 374 galaxies.

3.1. The Relationship between X-Ray and Optical Emission

In this section, we address whether we can recover AGNs that are absorbed at X-ray wavelengths by comparing L_X and $L_{[O\,III]}$ measurements for our samples of X-ray and optical AGNs.

The [O III] $\lambda 5008$ line, as one of the strongest narrow optical emission lines, provides a robust tracer of AGN power and (at least at lower redshifts) is less contaminated by emission due to SF activity than the Hα line (e.g., Brinchmann et al. 2004; Heckman et al. 2004). The hard band X-ray emission is also a robust estimator of AGN power and can penetrate regions with low to moderate hydrogen column densities. However, X-ray emission will be suppressed in Compton-thick or highly obscured AGNs. Low-luminosity AGNs may also be missed due to the flux limit of the X-ray data especially toward the edges of the X-ray pointings.

In Figure 9 (left panel) we show $L_{[O\,III]}$ versus $L_{X(2-10\,keV)}$ for X-ray (blue circles) and optically selected (green circles) AGNs in MOSDEF. For the optical AGNs that do not have X-ray detections in the hard band, we use the upper limits on

$L_{X(2-10\,keV)}$ (at 95% confidence level). Here we consider only AGNs with significant [O III] $\lambda 5008$ detections.[6] The blue solid line shows the average $\log(L_X/L_{[O\,III]})$ for X-ray AGNs in MOSDEF. The dotted line shows the measurement of $\log(L_X/L_{[O\,III]})$ for an X-ray selected sample at $z < 0.2$ by Heckman et al. (2005).

We note that the AGN [O III] $\lambda 5008$ luminosity in our sample is corrected for dust reddening. To determine the correction factor, we calculate the color excess from the Balmer decrement and combine this with the value of the MOSDEF dust attenuation curve at 5008 Å (Reddy et al. 2015). This correction results in an average increase of ~ 0.17 dex in [O III] luminosity for the AGNs in our sample. The [O III] luminosities from Heckman et al. (2005) are not corrected for dust reddening. We also note that the X-ray selected AGNs in the Heckman et al. (2005) sample are detected in the 3–20 keV hard X-ray band, and we converted their luminosity to $L_{X(2-10\,keV)}$ assuming $\Gamma = 1.9$.

In the right panel of Figure 9 we show the distributions of $\log(L_X/L_{[O\,III]})$ for X-ray and optical AGN samples. For the X-ray selected AGNs in MOSDEF, the average $\log(L_X/L_{[O\,III]})$ is 1.40 dex (with a standard deviation of 0.44 dex). This measurement is consistent with the average ratio in Heckman et al. (2005) (1.73 dex with a standard deviation of 0.41 dex), considering the uncertainties and the lack of the reddening correction in Heckman et al. (2005). Trouille & Barger (2010) with a larger sample of X-ray selected AGNs at $z < 0.85$ also find a similar average $\log(L_X/L_{[O\,III]})$ (1.46 dex, with 0.6 dex standard deviation), and indicate that the fraction of X-ray AGNs that are not identified in optical diagnostics varies between 20% and 50% depending on the line used for

---

[6] The [O III] line for sources not shown in this figure is not necessarily low flux; in many cases it is simply impacted by a sky line. We also note that even if we do not detect [O III] for a given source, we can still in some cases optically identify it as an AGN, if it has a high [N II]/Hα ratio.

classifying optical AGNs (Kauffmann et al. 2003 versus Kewley et al. 2001). Trouille & Barger (2010) argue that this misidentification could be due to the complexity of the structure of the narrow-line region, which could result in escape of many of the ionizing photons, and therefore lower $L_{[O\,III]}$ in some sources.

Considering a sample of optically selected AGNs,[7] Heckman et al. (2005) find a large scatter in $\log(L_X/L_{[O\,III]})$ and identify a population of type 2 AGNs that are bright at [O III] $\lambda5008$ but under-luminous in X-ray. As shown in Figure 9, in MOSDEF we only identify two AGNs with low $\log(L_X/L_{[O\,III]})$ indicating the X-ray emission is heavily obscured.

The bulk of optically selected AGNs in our sample have a similar $\log(L_X/L_{[O\,III]})$ to the X-ray selected sample. The majority of optically selected AGNs with limits on L_X still follow the overall $\log(L_X/L_{[O\,III]})$ trend and are consistent with being intrinsically lower-luminosity AGNs. Thus at $z \sim 2$ the optical selection method is effective at identifying lower-luminosity AGNs that may be missed by X-ray surveys due to the limited (and variable) depth of the X-ray data. However, deeper X-ray data could reveal that these sources are under-luminous at X-ray wavelengths and thus are candidate obscured AGNs.

Overall, we find that the relationship between L_X and $L_{[O\,III]}$ in our sample at $z \sim 2$ is consistent with that of the Heckman et al. (2005) local X-ray AGN sample. However, only $\sim 50\%$ of our optically selected AGNs are detected at X-ray wavelengths (see also Figure 5). In part, this is due to the fact that the X-ray data do not have uniform depth across our fields, unlike the more uniform [O III] sensitivity in the MOSDEF spectra. Thus, at these redshifts, optical selection may be more effective at identifying AGNs, especially lower luminosity sources, but does not obviously identify significant populations of heavily absorbed AGNs. We also find that $\sim 75\%$ of the X-ray AGNs are selected at optical wavelength, indicating that optical selection is relatively complete but can miss some AGNs that are found by X-ray surveys. This is mainly due to contamination of the optical spectra at $z \sim 2$ from the sky lines, as we discuss below in Section 4.1.

3.2. AGN Luminosities and Specific Accretion Rates

To further investigate the differences between AGN samples identified at different wavelengths at $z \sim 2$, in Figure 10 we compare the distributions of AGN luminosities (left panels), host stellar masses (central panels), and specific accretion rates (right panels) for our samples of X-ray AGNs (blue), IR AGNs (red) and optical AGNs (green). In the middle panels, we additionally show the rescaled histogram of the stellar mass distribution of our entire galaxy and AGN sample that includes 531 sources in gray. In the top row of Figure 10, we show only those sources with a significant [O III] flux in the MOSDEF data (and thus measured $L_{[O\,III]}$), which results in a sample of 34 sources. In the bottom row of Figure 10, we show only those sources with a significant hard X-ray detection (and thus measured L_X), resulting in a sample of 16 sources (after excluding broad-line AGNs and sources with soft band detections only). As noted above, a single source can be identified as an AGN at X-ray, IR, and optical wavelengths, therefore the same object can be included in multiple

distributions here. By construction, all sources in the bottom panels are identified as X-ray AGNs, whereas in the top panels we include sources identified as X-ray and IR AGNs where we are able to measure $L_{[O\,III]}$ but do not identify the source as an AGN based on our BPT diagnostics.

The specific accretion rate (shown in the right panels of Figure 10) traces the rate of SMBH growth relative to the stellar mass of the host galaxy, providing an indicator of how rapidly a galaxy is growing its black hole (see Aird et al. 2012). By calculating specific accretion rates, we can account for any differences in the stellar masses of the host galaxies of AGNs selected at different wavelengths, revealing differences in the types of AGNs that are selected with each method that may not be apparent from the observed luminosities.

The specific accretion rate is calculated from either the $L_{[O\,III]}$ or L_X and is given by

$$\lambda_{\text{band}} = \frac{k_{\text{band}} L_{\text{band}}}{1.3 \times 10^{38} \times 0.002 \dfrac{M_*}{M_\odot}} \qquad (8)$$

where k_{band} is the corresponding bolometric correction. We adopt a single bolometric correction at each wavelength. At optical wavelengths we use a mean bolometric correction of 600 from Kauffmann & Heckman (2009), which corresponds to the mean correction for extinction-corrected [O III] $\lambda5008$ luminosity (see also Netzer 2009; LaMassa et al. 2010). For sources with X-ray detections we use a constant bolometric correction of $k_{X(2-10\ \text{keV})} = 25$. We also estimated the bolometric luminosity using the luminosity-dependent bolometric corrections from Hopkins et al. (2007) and Lusso et al. (2012) for type 2 AGNs, but this does not alter the overall trends seen in Figure 10 when using a single bolometric correction. The denominator in the above equation is chosen such that the units of λ_{band} approximately correspond to the Eddington ratio (assuming a single scaling between SMBH mass and total stellar mass).

For AGNs with significant [O III] detections, the median statistical uncertainties on $L_{[O\,III]}$, stellar mass, and $\lambda_{[O\,III]}$ are 0.04 dex, 0.10 dex, and 0.12 dex, respectively. For AGNs with X-ray detections, the median uncertainties on L_X, stellar mass, and λ_X are 0.20, 0.07, and 0.23 dex. However, there may be additional uncertainties in $\lambda_{[O\,III]}$ and λ_X from the bolometric corrections (which may depend on Eddington ratio, see Vasudevan & Fabian 2007) that could result in larger uncertainties.

We use a Kolmogorov–Smirnov (KS) test to compare the distributions shown in Figure 10 for the different AGN selections and assess if there are significant differences (requiring a p-value <0.05, corresponding to a $>2\sigma$ equivalent confidence level). Based on our KS tests, we find no evidence for significant differences in the distributions between any two samples, indicating that the distributions of luminosities, host stellar masses and specific accretion rates for X-ray, IR, and optical AGNs are all statistically consistent with being drawn from the same parent population.

However, the lack of significant differences could be due to our relatively small sample sizes. In Figure 10 there are indications of differences in these distributions, probed here for the first time at $z \sim 2$, that appear consistent with previously identified selection biases at lower redshifts (e.g., $z \sim 0.1$–1: Mendez et al. 2013). In general, there is a bias against AGN

---

[7] We note that the optical AGNs in Heckman et al. (2005) are selected based on an [O III] $\lambda5008$ flux limit rather than the BPT diagram.
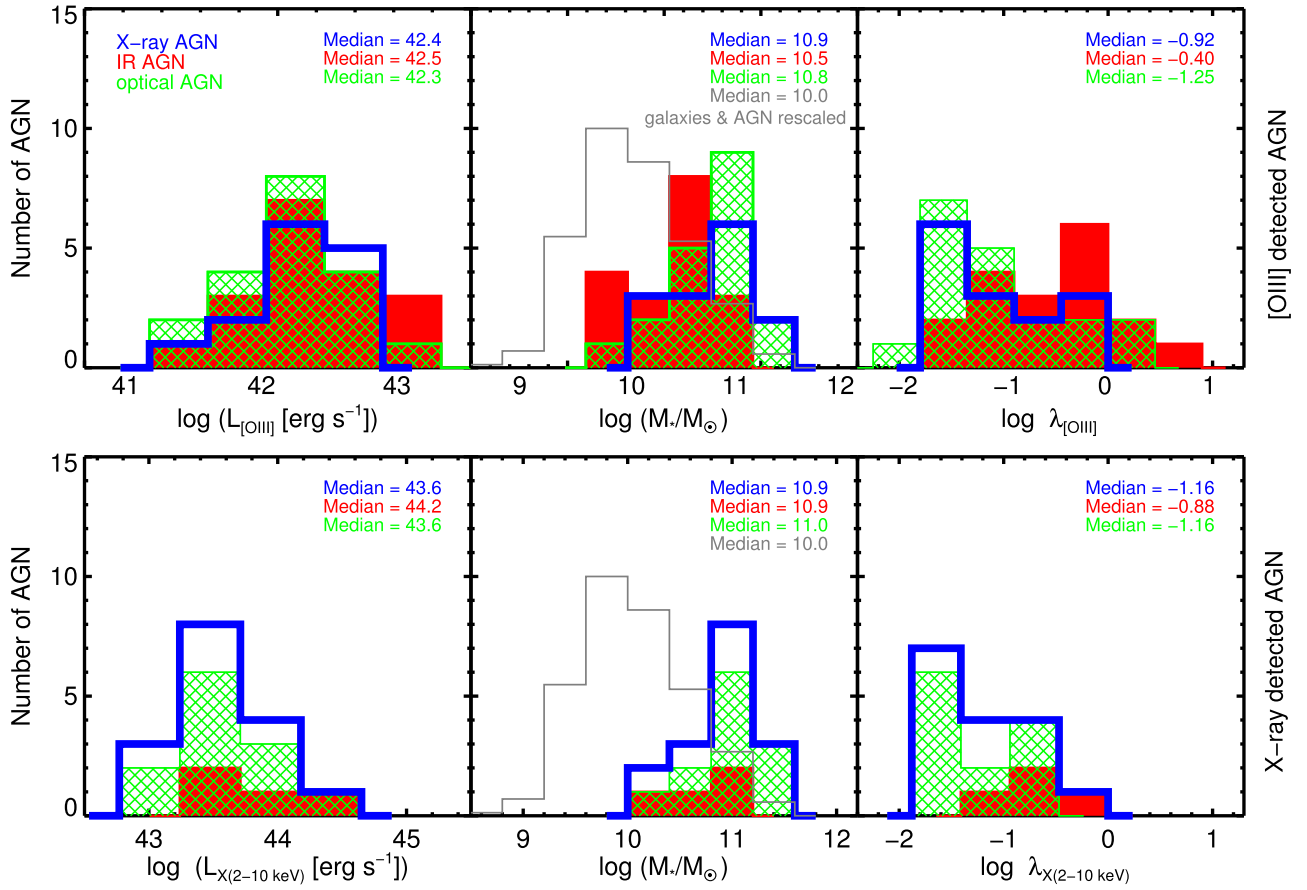
Figure 10. The observed luminosity (left), stellar mass (center), and specific accretion rates (right) distributions of X-ray (blue), IR (red), and optical (green) AGNs with significant [O III] detection in top row and significant hard X-ray detection in the bottom row. The median values are given in each panel. AGNs selected at all three wavelengths in our sample have very similar $L_{[\mathrm{O\,III}]}$ (and L_X) distributions (left panels). In the middle panels the gray histograms indicate the stellar mass distributions of our entire sample (galaxies and AGNs). The stellar mass distributions clearly reflect the bias against AGN identification in low-mass galaxies.

identification in relatively low-mass galaxies. For IR selection there may be an additional bias against the most massive galaxies in our sample. IR selection appears to identify AGNs with, on average, lower stellar masses and higher specific accretion rates i.e., sources where the light from the AGN dominates over the host galaxy.

X-ray selection is able to probe low specific accretion rates which may introduce a bias toward higher stellar mass host galaxies (e.g., Aird et al. 2012, due to the X-ray flux limits, low specific accretion rate sources will not be identified in lower mass galaxies). Optical selection—a key additional probe with our MOSDEF sample—appears to identify AGNs with similar properties to the X-ray selected population i.e., down to low specific accretion rates and generally in higher stellar mass galaxies.

Overall, our results show that with optical diagnostics we are able to identify less powerful, low accretion rate AGNs that may not be identified at other wavelengths (either due to obscuration or limited sensitivity). We also find that IR AGN selection preferentially identifies powerful AGNs that are hosted in relatively lower-mass galaxies, compared to optical and X-ray AGN selection. Each of these identification methods at different wavelengths are incomplete and suffer from selection biases, therefore a combination of identification methods can provide a more complete picture of AGN properties.

3.3. AGN Host Galaxy Properties

In this section we investigate the properties of the host galaxies of our AGN samples in more detail and compare with a sample of inactive galaxies from MOSDEF.

The MOSDEF galaxy sample spans a wide range in both SFR $\left(-1 \lesssim \log\left(\frac{\mathrm{SFR}}{\mathcal{M}_\odot\,\mathrm{yr}^{-1}}\right) \lesssim 3\right)$ and stellar mass $\left(8 \lesssim \log\left(\frac{\mathcal{M}_*}{\mathcal{M}_\odot}\right) \lesssim 12\right)$. From the data in the first two years of the MOSDEF survey, we identify 481 galaxies with an average stellar mass of $\sim 10^{10}\,\mathcal{M}_\odot$. While the AGN host galaxies span the full range of SFRs of the galaxy sample, they span a more limited range in stellar mass (less than two orders of magnitude) with an average stellar mass of $10^{10.6}\,\mathcal{M}_\odot$ for their host galaxies. The observational bias against AGN identification (at any wavelength) in low-mass galaxies restricts our AGN sample to relatively massive host galaxies (e.g., Aird et al. 2012).

Since stellar mass correlates with other physical properties such as metallicity, age, and SFR of the galaxy, we construct a stellar mass-matched control sample of inactive galaxies for comparative analysis with the AGN host galaxies. To create this sample, we bin the AGN host galaxies in narrow intervals of $\Delta \log\left(\frac{\mathcal{M}_*}{\mathcal{M}_\odot}\right) = 0.05$ dex and select 50 inactive galaxies from the full galaxy sample to create a sample with the same stellar mass distribution as the AGN host galaxies.
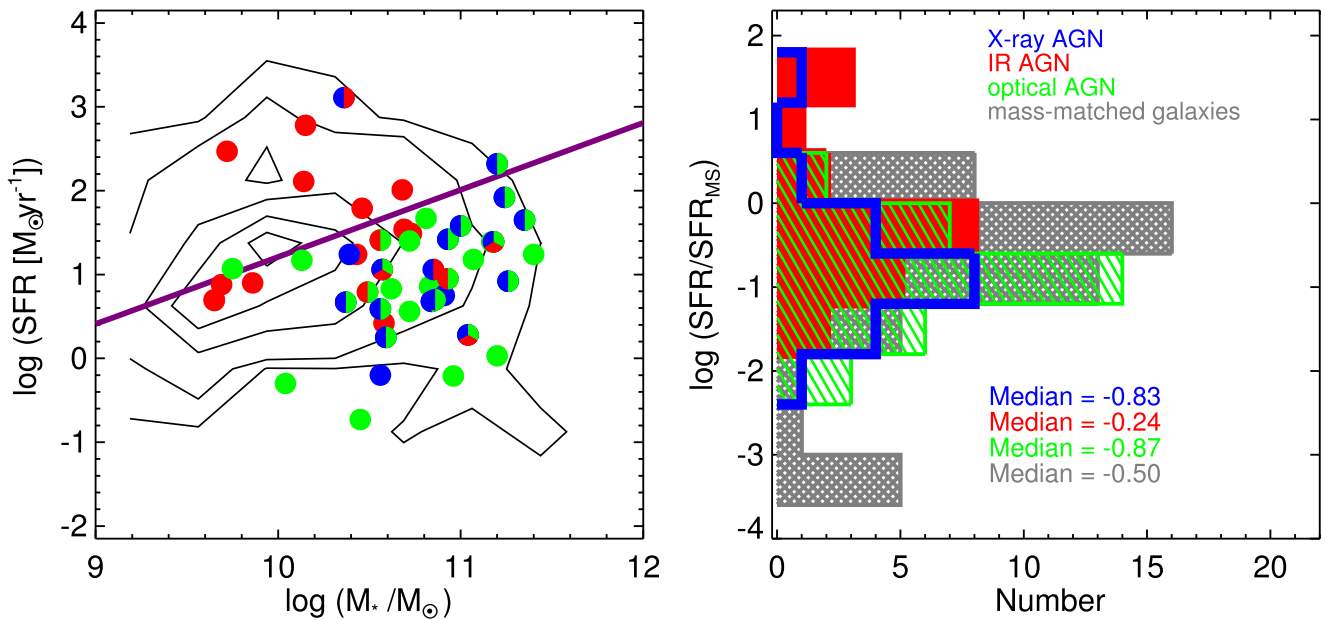
Figure 11. Left: SFR vs. stellar mass for the full MOSDEF galaxy sample (contours) and X-ray (blue), IR (red), and optically selected (green) AGN host galaxies. The purple line shows the relation from Shivaei et al. (2015) for the main sequence of SF of MOSDEF galaxies at $z < 2.6$. Compared to the full galaxy sample, AGN host galaxies span a similar range of SFR but a more limited range of stellar mass. Right: The SFR/SFR$_{MS}$ distributions in a stellar mass-matched inactive galaxy sample (gray) compared to the various AGN samples. The median SFR/SFR$_{MS}$ are given for each population. IR AGNs appear to be biased toward higher SFR/SFR$_{MS}$. Based on the KS test, we find that the IR AGNs have a different distribution of SFR/SFR$_{MS}$ (at the $>2\sigma$ equivalent confidence level) compared to either the optical AGNs ($p = 0.004$) or the X-ray AGNs ($p = 0.02$) samples.

In the left panel of Figure 11, we show the SFR versus stellar mass distributions of AGNs (colored points) in MOSDEF compared to the full galaxy sample (contours). There is a well known positive correlation between the SFR and stellar mass of galaxies, known as the "main sequence" of SF (e.g., Elbaz et al. 2007; Noeske et al. 2007; Karim et al. 2011; Whitaker et al. 2012; Shivaei et al. 2015). The purple line in this figure shows the relation for the main sequence of SF, based on SED fitting, for MOSDEF galaxies at $1.4 < z < 2.6$ from Shivaei et al. (2015):

$$\log\left(\frac{\text{SFR}}{\mathcal{M}_\odot \text{ yr}^{-1}}\right) = (0.80 \pm 0.05) \times \log\left(\frac{\mathcal{M}_*}{\mathcal{M}_\odot}\right) - (6.79 \pm 0.55). \tag{9}$$

Figure 11 shows that AGNs exist in galaxies over the full range of SFR probed by the MOSDEF sample. We find that the majority of optical and X-ray AGN host galaxies lie below the main sequence of SF, while IR AGN host galaxies are found both above and below the main sequence.

In the right panel of Figure 11, we show the distribution of SFR/SFR$_{MS}$ which is the relative offset of the SFR from the main sequence at the stellar mass of the host galaxy. We additionally show the SFR/SFR$_{MS}$ distribution for our mass-matched inactive galaxy sample. The median SFR/SFR$_{MS}$ for each sample is given in the figure. The median statistical uncertainty on log(SFR/SFR$_{MS}$) for AGNs is 0.23 dex and 0.34 dex for the mass-matched galaxies. A KS test shows that the SFR/SFR$_{MS}$ distribution of the AGN host galaxies is not significantly different from our stellar mass-matched inactive galaxy sample. We further consider three control samples of inactive galaxies, each mass-matched with AGNs identified at each wavelength, and compare the physical properties of individual AGN populations with their mass-matched galaxies. We find that the distribution of SFR/SFR$_{MS}$ for each AGN

sample is consistent with their inactive mass-matched galaxies. Comparing between the various AGN samples (using KS tests), we find that the distributions of SFR/SFR$_{MS}$ of X-ray and optical AGNs are statistically consistent with each other. However, we find the distribution of SFR/SFR$_{MS}$ for IR AGN is different at (at the $>2\sigma$ equivalent confidence level) compared to the optical AGNs ($p = 0.004$) or the X-ray AGNs ($p = 0.02$) samples.

To further investigate the host galaxy properties, we consider the rest-frame $U - V$ versus $V - J$ color diagram (*UVJ* color). This diagram is commonly used to distinguish quiescent galaxies from star-forming galaxies with different dust content (e.g., Williams et al. 2009; Whitaker et al. 2011; Muzzin et al. 2013). To estimate rest-frame colors we use the EAzY code (Brammer et al. 2008) by interpolating between the observed photometric bands (see Kriek et al. 2015), with the AGN contributions subtracted. In Figure 12 we show our AGNs (colored points) in *UVJ* space, along with mass-matched MOSDEF galaxies (contours). The dotted magenta line in this figure shows the region isolating the quiescent galaxies, identified using criteria from Williams et al. (2009):

$$U - V > 1.3, \tag{10}$$

$$U - V = 0.88 \times (V - J) + 0.69, \tag{11}$$

$$V - J < 1.6. \tag{12}$$

The cyan dotted line shows the demarcation from Kriek et al. (2015) that divides star-forming galaxies into those that are red and dusty from those that are blue and less dusty.

Table 1 indicates the fraction of AGNs in each region of *UVJ* space, compared to the fractions of our mass-matched galaxy sample that fall in each region. The errors on the fractions are estimated from bootstrap resampling. Given the errors, there is not a significant difference between the fractions of AGNs and mass-matched galaxies in different regions of *UVJ* space.

Table 1
The Fraction of AGNs and Stellar Mass-matched Galaxies in Different Parts of *UVJ* Space

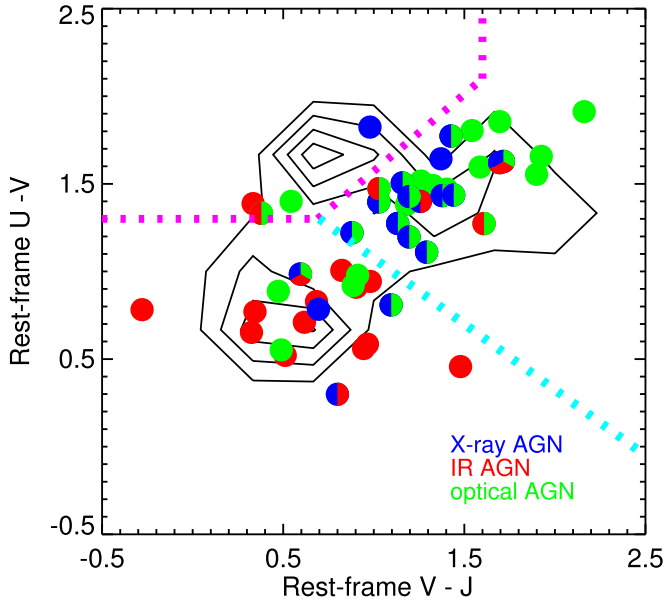| Region	AGN	Mass-matched Galaxies
quiescent	8% ± 4%	14% ± 4%
less dusty SF	39% ± 7%	49% ± 6%
dusty SF	53% ± 7%	37% ± 6%

Figure 12. The rest-frame $U - V$ vs. $V - J$ color diagram, where contours shows mass-matched inactive galaxies and the blue, red, and green circles show X-ray, IR, and optical AGNs. The dotted magenta line isolates quiescent galaxies using criteria from Williams et al. (2009), while the dotted cyan line shows the demarcation from Kriek et al. (2015) for dividing dusty vs. less dusty star-forming galaxies. Considering the errors in Table 1, the fraction of AGNs in each part is not significantly different than their mass-matched galaxies. Comparing the fraction of IR and optical AGNs indicates that a higher fraction of IR AGNs are in the less dusty star-forming region (at 3.8σ significance) and a higher fraction of optical AGNs are in the dusty star-forming region (at 4.2σ significance).

The location of galaxies in *UVJ* space depends sensitively on stellar mass; in particular within the star-forming population, dusty galaxies are more massive (e.g., Williams et al. 2010). Here, we find that AGNs have a similar distribution in *UVJ* space to a stellar mass-matched inactive galaxy sample. Figure 12 also shows that the majority of optical AGNs (73%) and X-ray AGNs (72%) are identified in dusty star-forming galaxies, while the majority of the IR AGNs are identified in less dusty star-forming galaxies (68%).

Considering the sensitivity of the *UVJ* diagram to stellar mass, and the fact that each AGN population has a different mass distribution, we compare the distribution of *UVJ* colors for each of our three AGN samples to an appropriately mass-matched galaxy sample. For the X-ray and IR AGN samples we find that their distribution in *UVJ* space is consistent with their corresponding mass-matched galaxy sample, indicating that the higher density of IR-AGNs in the non-dusty star-forming region in Figure 12 can be attributed to the lower stellar masses (on average) of the hosts of IR-selected AGNs. The fraction of optical AGNs in the dusty star-forming region is higher than their mass-matched galaxies (at 2.9σ significance), which we discuss below in Section 4.

In Figure 13 we compare the dust extinction and stellar age derived from SED fitting (after subtracting the AGN contribution) for AGN host galaxies with the mass-matched inactive galaxies. We illustrate the distributions of visual extinction (A_V) (left panel) and stellar age (middle panel) for AGNs and mass-matched galaxies. Additionally, we show the distributions of stellar age for individual AGN populations in the right panel. The median values of each distribution are given in the figure. The median statistical error on A_V is 0.40 mag for the AGN and 0.30 mag for the mass-matched galaxies. The median error on log(stellar age) is 0.30 dex for the AGNs and 0.13 dex for the mass-matched galaxies.

The full (non mass-matched) MOSDEF galaxy sample has a median $A_V = 0.5$ mag and a median stellar age of $10^{8.6}$ year, with distributions in A_V and stellar age that are significantly different from the AGN sample. The median dust extinction and age are very similar in AGN and mass-matched inactive galaxy populations, and KS tests show that the two populations do not have statistically different distributions in either parameter. The similarity of these distributions is not entirely unexpected, given that there are strong correlations between stellar mass and both extinction and stellar age.

We note that stellar age estimation is sensitive to various parameters in SED fitting, in particular, the SF history models. However, the distribution of τ (the characteristic SF timescale) for the MOSDEF AGNs is not significantly different from the distribution of τ for the mass-matched galaxies. We also find a similar *joint* distribution in stellar age and dust extinction between the AGN and mass-matched galaxies, in that galaxies with younger stellar populations are dustier than galaxies with older stellar populations.

In the right panel of Figure 13 we show stellar age distributions for the separate AGN populations in our sample and find a median stellar age of ~1.3 Gyr, 630 Myr and 1 Gyr, respectively, for X-ray, IR and optical AGNs. KS tests show a 2σ ($p = 0.02$) significance level difference in their age distributions that is most likely due to the stellar mass selection biases, with IR AGNs being identified in relatively lower mass galaxies, compared to optical and X-ray AGNs.

Overall, our results indicate that the distributions of SFR, dust, and stellar age in AGNs and mass-matched inactive galaxies are very similar, and that the key parameter in finding these similar distributions is the stellar mass of both populations. Stellar mass also plays an important role in AGN identification. While IR AGNs are biased against the most massive galaxies, we can identify them in less dusty galaxies with younger stellar population and relatively high SF activity. In contrast, optical AGN are identified in dusty massive galaxies with older stellar populations and lower SF activity.

3.4. The Relationship between SF and AGN Activity

We now investigate whether there is a connection between SF activity and AGN activity for individual sources in our $z \sim 2$ sample. To trace the AGN activity we use L_X for those AGNs with X-ray detections and $L_{[O III]}$ for AGNs with significant [O III] measurements. To quantify the relation between AGN luminosity and SFR, we calculate the correlation coefficient and the corresponding significance using the r $-correlate$ routine in IDL, which computes the Spearman's rank correlation coefficient (cc) and the significance of its deviation from zero (p).
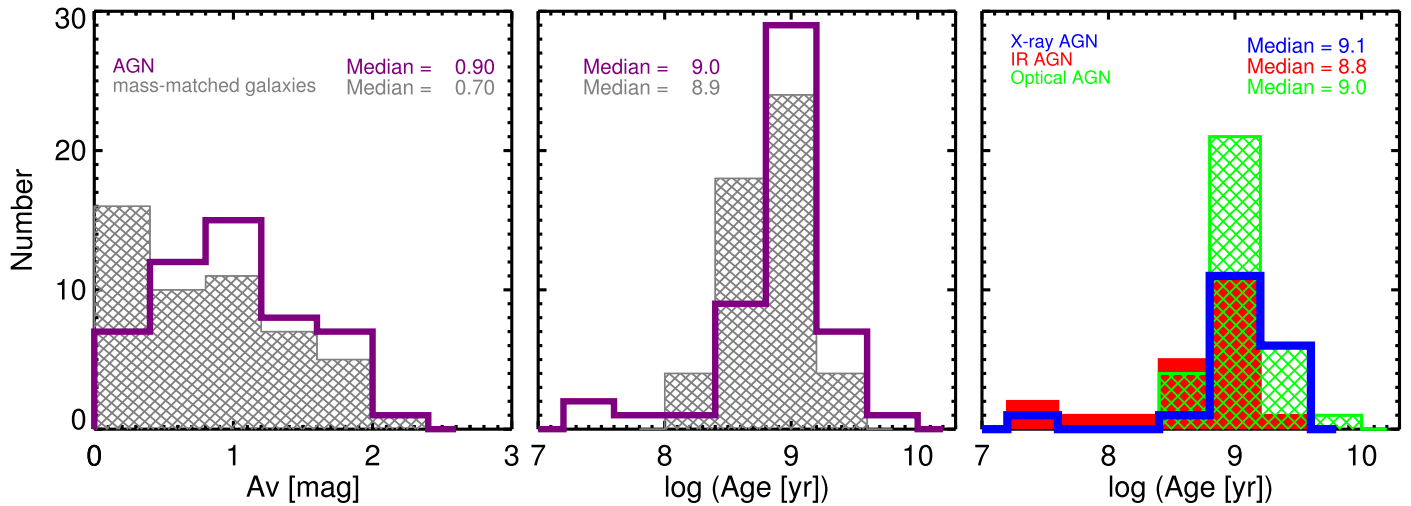
Figure 13. Left: The dust extinction (A_v) distributions; Middle: The stellar age distribution for full MOSDEF AGNs (purple) and mass-matched galaxy samples (gray). The KS test shows that the AGN and mass-matched galaxy samples have statistically similar A_v and age distributions. The median values with the standard errors are given for each population. Right: The stellar age distribution in each AGN population. IR AGNs reside in galaxies with younger stellar population compared to the optical AGN host galaxies at $>2\sigma$ significance ($p = 0.02$).

As noted in Section 3.3, the SFRs and stellar masses of galaxies are known to be correlated (e.g., Elbaz et al. 2007; Karim et al. 2011; Shivaei et al. 2015). Therefore an underlying correlation between AGN luminosity and host galaxy stellar mass, if it existed, could result in a correlation between SFR and AGN luminosity. To take this stellar mass-dependent effect into account, instead of quantifying any correlation between SFR and AGN luminosity, we use SFR/SFR$_{MS}$ (the relative offset of the SFR from the main sequence at the stellar mass of the host galaxy). We use Equation (9), which defines the star-forming main sequence for the MOSDEF sample for galaxies at $1.4 < z < 2.6$ from Shivaei et al. (2015).

In Figure 14, we show SFR/SFR$_{MS}$ versus L_X for X-ray AGN host galaxies in the top left panel and stellar mass versus L_X in the lower left panel. The right panels show SFR/SFR$_{MS}$ versus $L_{[O III]}$(top) and stellar mass versus $L_{[O III]}$(bottom) for AGNs with 3σ [O III] detections. We also show the median SFR/SFR$_{MS}$ and stellar mass in bins of L_X and $L_{[O III]}$ with the black stars, where the error bars indicate the standard deviation of the median in each luminosity bin. As shown in the figure, we find no significant correlation between SFR/SFR$_{MS}$ and either L_X or $L_{[O III]}$.

We note again that we have not accounted for any contribution to $L_{[O III]}$ from SF in our sample, as we are unable to correct for this on a source by source basis. In general, there is a positive correlation between SFR and [O III] emission in the galaxy population (e.g., Mehta et al. 2015). Although we do not find a significant correlation between SFR/SFR$_{MS}$ and $L_{[O III]}$ here, the possible contribution from SF to $L_{[O III]}$ could produce a correlation and should thus be considered in any future studies with larger samples.

Overall, we do not find any significant correlations between SFR and AGN luminosity in our sample. However, a common gas supply for triggering and fueling both of these phenomena could play an important role in galaxy and AGN growth. With a larger sample (and the possibility of correcting $L_{[O III]}$ for SF contributions), the connection between the growth of SMBHs and their host galaxies can be investigated more accurately.

4. DISCUSSION

In this paper we use data from the first two years of the MOSDEF survey, which includes 55 AGNs identified with X-ray, IR, and/or optical diagnostics at $z \sim 2$.

We investigate the selection of these AGNs and their host galaxies properties. Below we first discuss the uniqueness and overlap of AGN identification at different wavelengths and summarize the selection biases of each identification method. We further compare the host galaxy properties of the AGNs in our sample with other studies in the same redshift regime. Finally, we discuss our ability to probe the coeval growth of SMBHs and galaxies at $z \sim 2$ with this data set.

4.1. Uniqueness and Overlap of AGNs Identified at Different Wavelengths

Our sample of 55 AGNs at $z \sim 1.4$–3.8 identified using X-ray, IR, and/or optical diagnostics allows us to quantify the uniqueness and overlap of AGN selection at different wavelengths. The numbers of AGNs identified at different wavelengths and the overlap between the samples are shown by the Venn diagram in Figure 5. As shown in this figure, roughly half of the IR AGN sample and almost half of optical AGN sample are *not* identified as AGNs at the other wavelengths. X-ray AGN identification provides important confirmation of AGNs selected at other wavelengths, but in our sample it does not uniquely identify many additional AGNs to those identified at MIR and optical wavelengths.

The number of AGNs recovered at each wavelength depends on the depth of the observational data available at that wavelength. To investigate the differing depths of our observations, we compare the bolometric luminosity for AGNs identified at each wavelength. We adopt a single bolometric correction at each wavelength. As mentioned in Section 3.1, we adopt $k_{X(2–10 keV)} = 25$ and $k_{[O III]} = 600$ respectively for sources with X-ray detections and significant [O III] detections. At MIR wavelengths we adopt the average bolometric correction from Richards et al. (2006) at 5.8 μm, giving $k_{IR} = 8$. Although a single bolometric correction is likely an oversimplification, it is sufficient for our purposes to compare
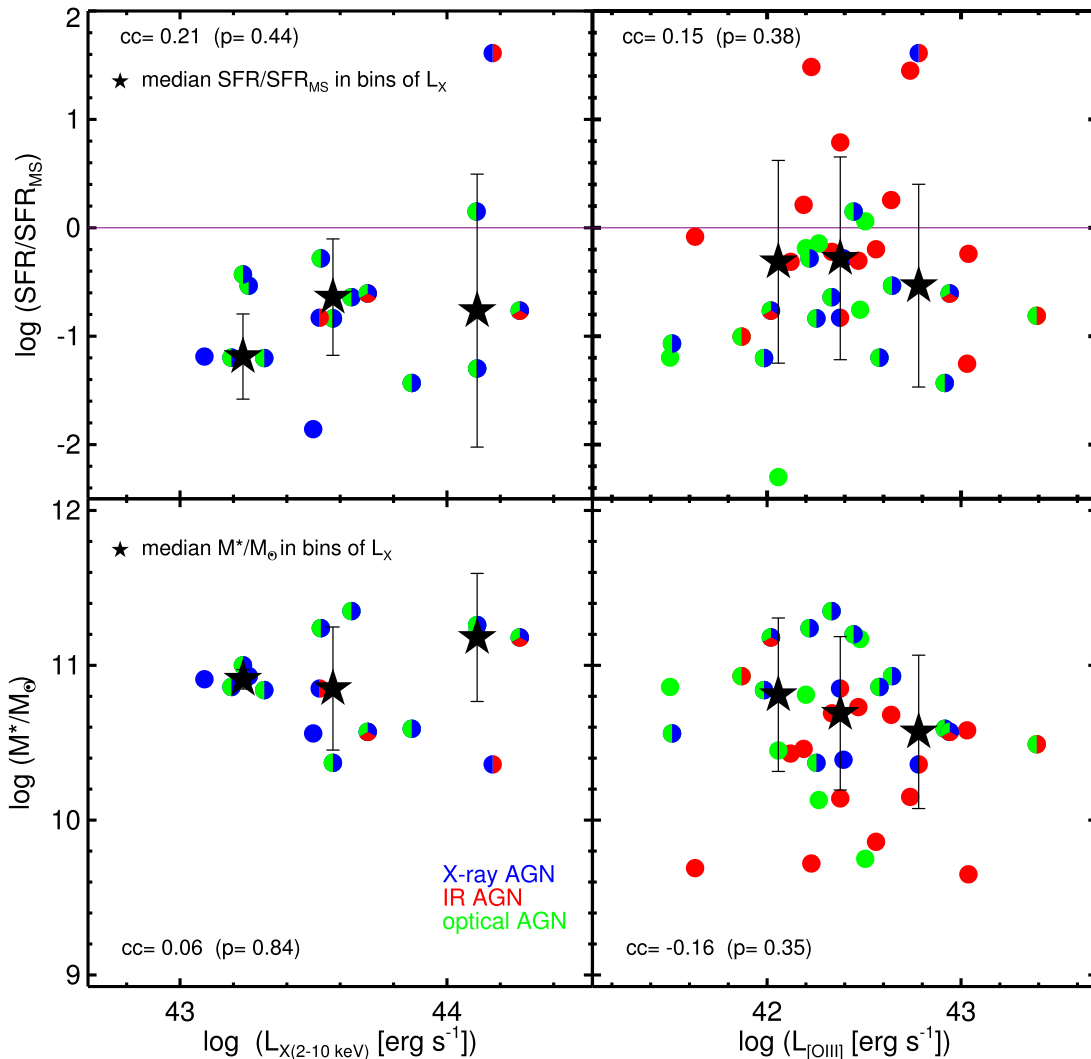
Figure 14. Left: The AGN host galaxy SFR relative to the main sequence of SFR (SFR/SFR$_{MS}$, top) and host galaxy stellar mass (bottom) as a function of L_X (left) and $L_{[O\,III]}$ (right, for AGNs with significant [O III] detections). The X-ray, IR and optical AGNs are shown respectively with blue, red, and green circles; the black stars indicate the median SFR/SFR$_{MS}$ and stellar mass in bins of L_X (or $L_{[O\,III]}$), with the error bars showing the standard deviation on the median values. The purple horizontal line in the upper panels shows the main sequence of SF, based on SED fitting, for MOSDEF galaxies at $1.4 < z < 2.6$ from Shivaei et al. (2015), used here to define a SFR/SFR$_{MS}$ of zero. The correlation coefficients are given in each panel.

the effective depths of the data at different wavelengths. The median bolometric luminosities are $L_{bol(X)} = 10^{45.1}$ erg s^{-1} for sources with X-ray detections, $L_{bol([O\,III])} = 10^{45.2}$ erg s^{-1} for sources with significant [O III] detections and $L_{bol(IR)} = 10^{45.3}$ erg s^{-1} for sources with 5.8 μm detections. The similar median bolometric luminosities indicate that our data are reaching similar depths at each wavelength. However, there are AGNs identified at a single wavelength that are not recovered at other wavelengths. Are these AGNs intrinsically less luminous at other wavelengths or is their unique identification due to another observational bias?

While X-ray imaging is a robust method for identifying AGNs with hydrogen column densities up to $N_H \approx 10^{23-24}$ cm^{-2}, X-ray emission cannot penetrate higher column densities and will therefore not identify Compton-thick AGNs. In addition, variation of the depth of *Chandra* observations in our various fields as well as a changing effective depth within a field results in a non-uniform flux limit (see, e.g., Mendez et al. 2013). Therefore, X-ray imaging may miss AGNs that are identified at other wavelengths. Furthermore, X-ray selection is

not expected to identify many AGNs that cannot be recovered at other wavelengths with sufficiently deep data. Indeed, in MOSDEF we find that the majority (87%) of X-ray AGNs are also recovered with IR or optical methods.

We find that 75% of our X-ray AGNs are recovered at optical wavelengths. There are six X-ray AGNs that are *not* identified at optical wavelengths: four of these sources have low S/N optical emission lines that are contaminated by sky lines; one of these sources is at $z > 3$ where Hα and [N II] fall beyond the wavelength coverage of MOSFIRE and therefore cannot be placed on the BPT diagram, and one source is on the star-forming sequence in the BPT diagram, indicating that it has a high SFR relative to the AGN luminosity and could therefore not be identified as an optical AGN. We thus conclude that optical AGN selection could identify the majority of X-ray selected AGNs and is mainly limited by the quality of the spectroscopic data. However, this method is likely biased against AGNs in host galaxies with high SFRs (e.g., Coil et al. 2015) as sources with higher SFR move toward the SF locus on the BPT diagram.

Table 2
The Selection Biases of X-ray, IR, and Optical AGN Host Galaxies in MOSDEF

Host Galaxy Property	X-ray AGN	IR AGN	Optical AGN
Stellar mass	bias toward high mass galaxies	bias toward moderate mass galaxies	bias toward high mass galaxies
SFR	no bias	bias toward relatively higher SFR	bias toward relatively lower SFR
Dust	possible bias toward higher dust content	possible bias toward lower dust content	possible bias toward higher dust content

Slightly less than half (42%) of the optical AGNs in our sample are not identified at X-ray or IR wavelengths, the majority in fields with relatively shallow X-ray data. These differences likely reflect the non-uniform depths probed by the X-ray data, compared to the fairly uniform depth at [O III] probed with the MOSDEF spectra. Also, as the Donley et al. (2012) selection is very incomplete, these optical AGNs are not identified using our IR selection criteria. Thus, optical selection can potentially identify substantial populations of AGNs that are missed at other wavelengths.

There are 13 IR AGNs in our sample that are not selected at X-ray or optical wavelengths. Although these sources have significant [O III] fluxes, they cannot be classified as optical AGNs for various reasons. All of these sources either do not have observations of Hα and [N II] (typically because they are at $z \gtrsim 3$) or have sky line contamination such that their [N II]/Hα ratio cannot be measured. Based on our upper limits on X-ray luminosities, it appears that these 13 IR AGNs are not identified at X-ray wavelengths due to the depths of the available X-ray data; indeed, 11 of these sources are in the COSMOS and AEGIS fields, where we have shallower X-ray data. Thus, IR AGN selection does *not* appear to identify a substantial AGN population (such as heavily obscured sources) that cannot be identified at other wavelengths. However, IR selection provides a more uniform depth than X-ray selection and is not affected by the data quality issues that impact optical selection; thus IR selection can be used to improve the completeness of AGN samples.

Mendez et al. (2013) reached similar conclusions regarding IR AGN selection using a larger sample of AGNs at intermediate redshifts ($z < 1.2$), finding that 90% of IR AGNs identified with shallow IR data are detected with sufficiently deep X-ray data. As the depth of the IR observations increases, Mendez et al. (2013) find that the fraction of IR AGNs that are *not* recovered by X-rays also increases, reflecting the additional IR AGN samples that are identified with extremely deep IR data. Using deep IR data, Donley et al. (2012) find that just 38% of IR AGNs in their sample are recovered at X-rays wavelengths, although as the depth of the X-ray data increases this fraction increases to 52% (see also Donley et al. 2007; Hickox et al. 2009). More recently, Cowley et al. (2016) find X-ray counterparts for only ∼22% of their IR AGNs. Cowley et al. (2016) use the Messias et al. (2012) redshift-dependent IR AGN selection criteria; thus the lower fraction of X-ray counterparts in their work could be either due to shallower X-ray data or the different IR selection method used.

4.2. AGN Selection Biases

As shown above and elsewhere, there are substantial observational selection biases in AGN samples identified at different wavelengths. These biases impact the observed properties of the AGN host galaxies identified.

In terms of X-ray identification, our results indicate that X-ray selection can identify AGNs at low specific accretion rates, which results in a selection bias toward massive host galaxies (see Figures 10 and 11). Indeed, previous studies have extensively shown that AGN identification *at any wavelength* is biased against low-mass galaxies (e.g., Kauffmann et al. 2003; Xue et al. 2010; Aird et al. 2012). This bias has also been seen in various studies of X-ray AGN host galaxies (e.g., Alonso-Herrero et al. 2008; Aird et al. 2012; Azadi et al. 2015). In terms of SF activity of X-ray AGN hosts, although they are mostly located below the main sequence of SF, their SFR distribution is not significantly different from that of inactive galaxies with a similar mass distribution, as most galaxies at that high stellar mass are also below the main sequence.

In terms of IR AGN identification, IR AGN selection is biased toward identifying AGNs with high specific accretion rates where the AGN IR light dominates over the host galaxy light (Mendez et al. 2013). This selection bias can result in identifying more luminous AGNs in moderately massive host galaxies. Using a larger sample at intermediate redshifts, Mendez et al. (2013) find that IR AGN selection mainly identifies high X-ray luminosity AGNs, while X-ray selection identifies AGNs with a wider range of luminosities. Given that most IR AGNs in our sample are not detected at X-ray wavelength we cannot make such a comparison here. We further find that within MOSDEF, IR AGNs are found in less dusty host galaxies with relatively younger stellar populations and higher SFRs. This effect can be understood as related to the stellar mass selection biases for IR AGNs: these are identified in lower stellar mass galaxies (compared to X-ray or optical AGNs) that tend to have less dust and younger stellar populations than higher mass galaxies.

In terms of optical AGN identification, we find that optical selection can identify lower accretion rate AGNs that may not be recovered at other wavelengths. Considering the similar $L_{[O\,III]}$ distributions for the various AGNs in our sample, this trend is driven by the high stellar masses of the optical AGN host galaxies (see also Coil et al. 2015), similar to X-ray AGNs. We further find that optical AGNs reside in dusty galaxies with older stellar populations and relatively moderate SF activity (median $\log(\mathrm{SFR}/\mathrm{SFR_{MS}}) = -0.87$ dex). The higher stellar mass of the optical AGN host galaxies leads to a bias toward higher dust content. It is also more likely for optical AGNs to be identified in galaxies with older stellar populations and lower SFR in the BPT diagram (Coil et al. 2015). We further note that the bias toward more massive host galaxies leads to a bias toward higher metallicities, therefore the optical selection method may not be successful in identifying low-mass–low-metallicity host galaxies (e.g., Groves et al. 2006). We

emphasize that although our sample is small, the selection biases of optical AGNs against lower-mass galaxies with higher SFR has been also reported in studies of optical AGNs at lower redshifts with large samples (Kauffmann et al. 2003; Trump et al. 2015).

Overall, we find that compared to IR and optical AGN selection techniques, X-ray identification is the least biased, with only a bias toward high stellar mass (but no additional SFR bias). We summarize the various selection biases discussed above in Table 2.

4.3. MOSDEF Host Galaxy Properties Compared to the Literature

In this study, we find no significant differences between MOSDEF AGN host galaxies and inactive galaxies of the same stellar mass. In particular, we find no significant differences between the SF activity of AGN host galaxies with the inactive mass-matched galaxies for AGN selected at a given wavelength. Thus, after taking into account of the observational selection biases, we find no evidence that AGN activity is preferentially occurring in a particular type of galaxy, although our relatively small sample size may preclude us from identifying weak trends.

The same result has been seen in some recent studies, e.g., Rosario et al. (2015) find a similar SFR distribution in X-ray AGN hosts and mass-matched galaxies at $z \sim 2$. Bongiorno et al. (2012) also find similar distribution of sSFR for AGNs and the inactive galaxies with a slight increase in AGN fraction toward lower sSFR. On the other hand, a number of studies find that AGNs are preferentially found in star-forming (main sequence) galaxies at these redshifts. Azadi et al. (2015) perform X-ray sensitivity corrections and find that X-ray AGNs are 2–3 times more likely to be found in galaxies with elevated SFR (see also Aird et al. 2012; Harrison et al. 2012; Santini et al. 2012; Bernhard et al. 2016). Recently, Mullaney et al. (2015) use *Herschel* and *ALMA* measurements and find that the majority of X-ray AGNs are *below* the main sequence of SF, arguing that studies using mean-stacking for SFR measurements can overestimate the level of SF in the host galaxies.

The MOSDEF sample does not contain a large number of quiescent galaxies, which lack high-S/N emission lines at the observed wavelengths of the survey (Kriek et al. 2015). However, the fraction of our AGNs in the quiescent region of *UVJ* space is similar to the fraction of mass-matched galaxies in that region. With a small number of quiescent galaxies in our sample, the majority of our AGNs are in star-forming galaxies which is consistent with the results from other studies at $z \sim 2$. However, to robustly determine whether AGN host galaxies lie preferentially below, above, or along the main sequence of SF will require larger samples for investigation.

Ellison et al. (2016) considered a sample of multi-wavelength identified AGNs at $z \sim 0$ and, similar to our results, find IR AGNs in galaxies with elevated SFR relative to the main sequence and optical AGNs in galaxies with lower SFR than the main sequence. Cowley et al. (2016) performed a similar analysis at $z \lesssim 3$, and find that the specific SFR $\left(\text{sSFR}, \frac{\text{SFR}}{\mathcal{M}_*} \right)$ in AGN host galaxies is, on average, higher than in mass-matched galaxies at $z \gtrsim 2$ for their IR selected AGN sample. No significant differences in sSFR were found for X-ray or radio AGN at these redshifts.

However, in our sample we find a similar sSFR distribution for IR AGNs and mass-matched galaxies. As IR AGNs in MOSDEF span a similar range of stellar mass as those identified in Cowley et al. (2016), the higher sSFR in Cowley et al. (2016) must be due to a higher SFR for IR AGNs in their sample. Additionally, our investigation shows that the majority of IR AGNs in our sample reside in less dusty star-forming galaxies, while Cowley et al. (2016) at $z \gtrsim 2$ find the majority of IR AGNs in dusty star-forming galaxies. The different SFR and dustiness of IR AGN in our sample compared to Cowley et al. (2016) could be due to the fact that they use a combination of IRAC and 24 μm observations for IR AGN identification (see Messias et al. 2012).

We further used the location of AGN host galaxies in *UVJ* space to investigate their dust properties. The location of galaxies in *UVJ* space is very sensitive to stellar mass, with lower-mass galaxies residing preferentially in the less dusty star-forming region, and more massive star-forming galaxies in the dusty region (e.g., Whitaker et al. 2011). While the full AGN sample used here shows a similar distribution as mass-matched inactive galaxies in *UVJ* space, we find that the fraction of optical AGNs in the dusty star-forming region is higher than their inactive mass-matched galaxies at the 2.9σ level. However, the X-ray and IR AGNs show a very similar behavior to their mass-matched galaxies. Although our optical AGN hosts are predominantly in dusty star-forming galaxies, we note that the A_V of these optical AGN hosts is not significantly higher than in the mass-matched galaxies or non-optical AGN population. Therefore, the difference in the fraction of optical AGNs and their mass-matched galaxies in the *UVJ* diagram could be a statistical fluctuation, rather than due to any intrinsic difference in dust content of the optical AGN host galaxies.

Overall, the AGNs in our sample have very similar physical properties to those of mass-matched inactive galaxies. At these redshifts, a larger sample of both quiescent galaxies and AGNs are required to study any potential differences between the SFR or dustiness of AGN hosts and inactive galaxies more robustly.

4.4. Are the Growth of Black Holes and the Growth of Their Host Galaxies Correlated at $z \sim 2$?

As discussed in the introduction, the global SMBH accretion rate density and SFR density both peak at $z \sim 2$–3 (e.g., Aird et al. 2015), which indicates that globally there is a relation between the growth of SMBH and their host galaxies. But the question still remains whether such a correlation exists on the scale of individual host galaxies. Our results indicate that SFR/SFR$_{\text{MS}}$ and AGN luminosity are not significantly correlated within our sample, using either L_X or $L_{\text{[O III]}}$ as a probe of AGN activity. Why then, given the similarity in the global scaling relations, do we not find a correlation?

Due to their stochastic fueling (e.g., Ulrich et al. 1997; Peterson 2001), the luminosities of AGNs may undergo dramatic changes in a short timescale (Keel et al. 2012), while SF activity remains stable in the host galaxies over long timescales (e.g., Wong 2009; Hickox et al. 2012). Therefore rapid AGN variability can play an important role in washing out any underlying trend that may exist between SFR/SFR$_{\text{MS}}$ and AGN luminosity. In fact, studies using average AGN luminosity in bins of SFR, instead of the luminosity of individual AGNs, find a positive trend between AGN luminosity and SFR of the host galaxy. (e.g., Chen

et al. 2013; Hickox et al. 2014; Azadi et al. 2015; Dai et al. 2015).

Although the connection between galaxy-wide SF and AGN activity might be hidden due to the variable nature of AGNs, Diamond-Stanic & Rieke (2012) find evidence of a strong correlation between AGN luminosity and SFR in the circumnuclear regions ($r < 1$ kpc). Thus, while our results do not show a significant correlation between the large-scale SF and AGN activity, these phenomena may have an underlying connection through a common gas supply. We note that violent events such as major mergers can provide a gas influx to fuel both AGN activity and SF. However, the moderate luminosity of AGNs in our sample indicates that these sources are generally at lower luminosities than those thought to be triggered by major mergers (e.g., Schawinski et al. 2012; Treister et al. 2012).

As discussed above in Section 2.6, AGNs and SF activity in the host galaxy can both contribute to the [O III] luminosity. In the local universe studies have proposed various methods for estimating the contribution from SF to the [O III] emission line (e.g., Kauffmann & Heckman 2009; Wild et al. 2010; Tanaka 2012). At the redshifts and depth of the MOSDEF survey only a fraction of our AGNs can be accurately placed on the BPT diagram, due to contamination from sky lines and the lack of spectroscopic wavelength coverage at higher redshifts. Therefore, the commonly used methods for estimating the SF contribution to $L_{\text{[O III]}}$ at low redshifts cannot be applied to our sample. Although $L_{\text{[O III]}}$ can be boosted by SF activity, here we do not find a significant correlation between SFR and $L_{\text{[O III]}}$, which indicates that it is unlikely for the instantaneous SFR to be correlated with $L_{\text{[O III]}}$.

5. SUMMARY

In this paper we use the data from the first two years of the MOSDEF survey to investigate AGN identification and their host galaxies' properties at $1.37 < z < 3.80$, with the majority of our sample at $z \sim 2$. We identify 55 AGNs using the X-ray imaging data from *Chandra*, MIR data from IRAC camera on *Spitzer*, and rest-frame optical spectra from the MOSDEF survey. We investigate the selection biases from each identification method and explore the host galaxy properties of these AGNs. We further consider the relation between SF activity and AGN luminosity in our sample. Our main conclusions are as follows.

1. We find that AGNs identified at any wavelength are biased against low-mass host galaxies; this is an observational selection bias. IR AGN identification has an additional bias against the most massive galaxies. Quantifying the SFR relative to the main sequence and comparing the distributions for IR and optical AGNs, we find that IR AGNs are primarily identified in galaxies with relatively higher SFRs, while optical AGNs are identified in galaxies with relatively lower SFRs ($p = 0.004$, at $>2\sigma$ significance). X-ray selection does not display any bias in the SFR distribution relative to the main sequence. The observational biases in stellar mass can result in biases in terms of the dust content of host galaxies, with IR AGNs showing a possible bias toward less dusty host galaxies and optical and X-ray AGNs showing a possible bias toward more dusty host galaxies in our sample.

2. Within the star-forming galaxy population, once stellar mass selection biases are taken into account, we find that AGNs reside in galaxies with similar physical properties (SFR, dust content, and stellar age) as inactive galaxies. Therefore we find no evidence of AGN activity in particular types of galaxies, which is consistent with stochastic fueling of AGNs in any kind of galaxy, and no strong evidence for AGN feedback.

3. The majority of the AGNs in our sample can be identified using optical diagnostics. We find that 75% of the X-ray AGNs in our sample are also identified with optical diagnostics, indicating the reliability of optical AGN selection. However, optical identification is limited by the quality of the spectroscopic data, as optical emission lines in most of the non-optical AGNs in our sample at $z \sim 2$ are contaminated by night sky lines.

4. Almost half of the IR AGNs in our sample are recovered at X-ray or optical wavelengths. IR imaging provides a more uniform depth than X-ray data and is not affected by the quality of optical spectroscopy; thus IR AGN identification can improve the completeness of AGN samples at $z \sim 2$.

5. The relationship between L_X and $L_{\text{[O III]}}$ in our sample at $z \sim 2$ is consistent with the relation of Heckman et al. (2005) in the local universe. Unlike Heckman et al. (2005), who found that the majority of local optical AGNs can be recovered at X-ray wavelengths, we find X-ray counterparts for only 50% of the optical AGNs in our sample. This is likely due to the relatively shallower and variable depth of the X-ray data across our fields.

6. We do not find a significant correlation between SFR/SFR_{MS} (SFR relative to the main sequence of SF) and AGN luminosity (using L_X or $L_{\text{[O III]}}$) in our sample. Although $L_{\text{[O III]}}$ can be boosted by SF activity in the host galaxy, at $z \sim 2$ we cannot apply correction techniques commonly used at lower redshifts to estimate the SF contamination.

Although the selection biases in our sample are derived from a small number of AGNs, they are consistent with results of studies at intermediate redshifts with larger samples. The presence of these selection biases indicates that in order to obtain a more complete AGN census, complementary identification techniques at multiple wavelengths are required. To robustly study AGN host galaxy properties, the selection biases from each identification technique should be taken into account.

References

Aird, J., Coil, A. L., Georgakakis, A., et al. 2015, MNRAS, 451, 1892
Aird, J., Coil, A. L., Moustakas, J., et al. 2012, ApJ, 746, 90
Aird, J., Nandra, K., Laird, E., et al. 2010, MNRAS, 401, 2531
Akylas, A., & Georgantopoulos, I. 2009, A&A, 500, 999
Alexander, D., & Hickox, R. 2012, NAR, 56, 93
Alexander, D. M., Bauer, F. E., Brandt, W. N., et al. 2011, ApJ, 738, 44
Alonso-Herrero, A., Pérez-González, P. G., Alexander, D. M., et al. 2006, ApJ, 640, 167
Alonso-Herrero, A., Pérez-González, P. G., Rieke, G. H., et al. 2008, ApJ, 677, 127
Assef, R. J., Kochanek, C. S., Ashby, M. L. N., et al. 2011, ApJ, 728, 56
Assef, R. J., Kochanek, C. S., Brodwin, M., et al. 2010, ApJ, 713, 970
Azadi, M., Aird, J., Coil, A. L., et al. 2015, ApJ, 806, 187
Baldry, I. K., Glazebrook, K., Brinkmann, J., et al. 2004, ApJ, 600, 681
Baldwin, J. A., Phillips, M. M., & Terlevich, R. 1981, PASP, 93, 5
Bell, E. F., McIntosh, D. H., Katz, N., & Weinberg, M. D. 2003, ApJS, 149, 289
Bernhard, E., Mullaney, J. R., Daddi, E., Ciesla, L., & Schreiber, C. 2016, MNRAS, 460, 902
Blanton, M. R., Hogg, D. W., Bahcall, N. A., et al. 2003, ApJ, 592, 819
Bongiorno, A., Merloni, A., Brusa, M., et al. 2012, MNRAS, 427, 3103
Boyle, B. J., & Terlevich, R. J. 1998, MNRAS, 293, L49
Brammer, G. B., van Dokkum, P. G., & Coppi, P. 2008, ApJ, 686, 1503
Brammer, G. B., van Dokkum, P. G., Franx, M., et al. 2012, ApJS, 200, 13
Brandt, W. N., & Alexander, D. M. 2015, A&ARv, 23, 1
Brightman, M., Nandra, K., Salvato, M., et al. 2014, MNRAS, 443, 1999
Brinchmann, J., Charlot, S., White, S. D. M., et al. 2004, MNRAS, 351, 1151
Brusa, M., Zamorani, G., Comastri, A., Hasinger, G., et al. 2007, ApJS, 172, 353
Buchner, J., Georgakakis, A., Nandra, K., et al. 2015, ApJ, 802, 89
Calzetti, D., Armus, L., Bohlin, R. C., et al. 2000, ApJ, 533, 682
Cardamone, C. N., Urry, C. M., Schawinski, K., et al. 2010, ApJL, 721, L38
Chabrier, G. 2003, PASP, 115, 763
Chen, C.-T. J., Hickox, R. C., Alberts, S., et al. 2013, ApJ, 773, 3
Ciliegi, P., Zamorani, G., Hasinger, G., et al. 2003, A&A, 398, 901
Coil, A. L., Aird, J., Reddy, N., et al. 2015, ApJ, 801, 35
Comastri, A., Ranalli, P., Iwasawa, K., et al. 2011, A&A, 526, L9
Conroy, C., Gunn, J. E., & White, M. 2009, ApJ, 699, 486
Cowley, M. J., Spitler, L. R., Tran, K.-V. H., et al. 2016, MNRAS, 457, 629
Daddi, E., Alexander, D. M., Dickinson, M., et al. 2007, ApJ, 670, 173
Dai, Y. S., Wilkes, B. J., Bergeron, J., et al. 2015, arXiv:1511.06761
Della Ceca, R., Severgnini, P., Caccianiga, A., et al. 2008, MmSAI, 79, 65
Diamond-Stanic, A. M., & Rieke, G. 2012, ApJ, 746, 168
Donley, J. L., Koekemoer, A. M., Brusa, M., et al. 2012, ApJ, 748, 142
Donley, J. L., Rieke, G. H., Pérez-González, P. G., & Barro, G. 2008, ApJ, 687, 111
Donley, J. L., Rieke, G. H., Pérez-González, P. G., Rigby, J. R., & Alonso-Herrero, A. 2007, ApJ, 660, 167
Elbaz, D., Daddi, E., Le Borgne, D., et al. 2007, A&A, 468, 33
Ellison, S. L., Teimoorinia, H., Rosario, D. J., & Mendel, J. T. 2016, MNRAS, 458, L34
Fazio, G. G., Hora, J. L., Allen, L. E., et al. 2004, ApJS, 154, 10
Ferrarese, L., & Merritt, D. 2000, ApJL, 539, L9
Fiore, F., Grazian, A., Santini, P., et al. 2008, ApJ, 672, 94
Gebhardt, K., Bender, R., Bower, G., Dressler, A., et al. 2000, ApJL, 539, L13

Genzel, R., Förster Schreiber, N. M., Rosario, D., et al. 2014, ApJ, 796, 7
Georgakakis, A., Pérez-González, P. G., Fanidakis, N., et al. 2014a, MNRAS, 440, 339
Georgakakis, A., Pérez-González, P. G., Fanidakis, N., et al. 2014b, MNRAS, 440, 339
Georgantopoulos, I., Georgakakis, A., Rowan-Robinson, M., & Rovilos, E. 2008, A&A, 484, 671
Gilli, R., Comastri, A., & Hasinger, G. 2007, A&A, 463, 79
Goulding, A. D., & Alexander, D. M. 2009, MNRAS, 398, 1165
Goulding, A. D., Forman, W. R., Hickox, R. C., et al. 2014, ApJ, 783, 40
Grogin, N. A., Kocevski, D. D., Faber, S. M., et al. 2011, ApJS, 197, 35
Groves, B. A., Heckman, T. M., & Kauffmann, G. 2006, MNRAS, 371, 1559
Hainline, K. N., Shapley, A. E., Greene, J. E., et al. 2012, ApJ, 760, 74
Hao, H., Elvis, M., Civano, F., & Lawrence, A. 2011, ApJ, 733, 108
Harrison, C. M., Alexander, D. M., Mullaney, J. R., Altieri, B., et al. 2012, ApJL, 760, L15
Harrison, C. M., Alexander, D. M., Mullaney, J. R., et al. 2016, MNRAS, 456, 1195
Heckman, T. M., & Best, P. N. 2014, ARA&A, 52, 589
Heckman, T. M., Kauffmann, G., Brinchmann, J., et al. 2004, ApJ, 613, 109
Heckman, T. M., Ptak, A., Hornschemeier, A., & Kauffmann, G. 2005, ApJ, 634, 161
Hernán-Caballero, A., Alonso-Herrero, A., Pérez-González, P. G., et al. 2014, MNRAS, 443, 3538
Hickox, R. C., Jones, C., Forman, W. R., et al. 2009, ApJ, 696, 891
Hickox, R. C., Mullaney, J. R., Alexander, D. M., et al. 2014, ApJ, 782, 9
Hickox, R., Wardlow, J., Smail, I., et al. 2012, MNRAS, 421, 284
Hopkins, P. F., Richards, G. T., & Hernquist, L. 2007, ApJ, 654, 731
Ivezić, Ž., Menou, K., Knapp, G. R., et al. 2002, AJ, 124, 2364
Juneau, S., Bournaud, F., Charlot, S., et al. 2014, ApJ, 788, 88
Juneau, S., Dickinson, M., Alexander, D. M., & Salim, S. 2011, ApJ, 736, 104
Karim, A., Schinnerer, E., Martínez-Sansigre, A., et al. 2011, ApJ, 730, 61
Kauffmann, G., & Heckman, T. M. 2009, MNRAS, 397, 135
Kauffmann, G., Heckman, T. M., Tremonti, C., et al. 2003, MNRAS, 346, 1055
Keel, W. C., de Grijp, M. H. K., Miley, G. K., & Zheng, W. 1994, A&A, 283, 791
Keel, W., Lintott, C., Bennert, K. S. V., et al. 2012, AJ, 144, 66
Kennicutt, R. C., Jr. 1998, ARA&A, 36, 189
Kewley, L. J., Dopita, M. A., Leitherer, C., et al. 2013, ApJ, 774, 100
Kewley, L. J., Dopita, M. A., Sutherland, R. S., Heisler, C. A., & Trevena, J. 2001, ApJ, 556, 121
Kewley, L. J., Geller, M. J., & Barton, E. J. 2006, AJ, 131, 2004
Klesman, A. J., & Sarajedini, V. L. 2012, MNRAS, 425, 1215
Koekemoer, A. M., Faber, S. M., Ferguson, H. C., et al. 2011, ApJS, 197, 36
Kormendy, J., Bender, R., & Cornell, M. 2011, Natur, 469, 374
Kriek, M., Shapley, A. E., Reddy, N. A., et al. 2015, ApJS, 218, 15
Kriek, M., van Dokkum, P. G., Labbé, I., et al. 2009, ApJ, 700, 221
Lacy, M., Storrie-Lombardi, L. J., Sajina, A., et al. 2004, ApJS, 154, 166
Laird, E. S., Nandra, K., Georgakakis, A., et al. 2009, ApJS, 180, 102
LaMassa, S. M., Heckman, T. M., Ptak, A., et al. 2010, ApJ, 720, 786
LaMassa, S. M., Heckman, T. M., Ptak, A., & Urry, C. M. 2013, ApJL, 765, L33
Lanzuisi, G., Ranalli, P., Georgantopoulos, I., et al. 2015, A&A, 573, A137
Lusso, E., Comastri, A., Simmons, B. D., et al. 2012, MNRAS, 425, 623
Magorrian, J., Tremaine, S., Richstone, D., et al. 1998, AJ, 115, 2285
Markwardt, C. B. 2009, arXiv:0902.2850
Masters, D., McCarthy, P., Siana, B., et al. 2014, ApJ, 785, 153
Mateos, S., Alonso-Herrero, A., Carrera, F. J., et al. 2012, MNRAS, 426, 3271
McLean, I. S., Steidel, C. C., Epps, H. W., et al. 2012, Proc. SPIE, 8446, 84460J
Mehta, V., Scarlata, C., Colbert, J. W., et al. 2015, ApJ, 811, 141
Meléndez, M., Heckman, T., Martínez-Paredes, M., Kraemer, S., & Mendoza, C. 2014, MNRAS, 443, 1358
Mendez, A. J., Coil, A. L., Aird, J., et al. 2013, ApJ, 770, 40
Messias, H., Afonso, J., Salvato, M., Mobasher, B., & Hopkins, A. M. 2012, ApJ, 754, 120
Mullaney, J. R., Alexander, D. M., Aird, J., et al. 2015, MNRAS, 453, L83
Mullaney, J. R., Pannella, M., Daddi, E., et al. 2012, MNRAS, 419, 95
Muzzin, A., Marchesini, D., Stefanon, M., et al. 2013, ApJ, 777, 18
Nandra, K., Georgakakis, A., Willmer, C., Cooper, M., et al. 2007, ApJL, 660, L11
Nandra, K., Laird, E. S., Aird, J. A., et al. 2015, ApJS, 220, 10
Netzer, H. 2009, MNRAS, 399, 1907
Neugebauer, G., Oke, J. B., Becklin, E. E., & Matthews, K. 1979, ApJ, 230, 79

Newman, S. F., Buschkamp, P., Genzel, R., et al. 2014, ApJ, 781, 21
Noeske, K. G., Weiner, B. J., Faber, S. M., Papovich, C., et al. 2007, ApJL, 660, L43
Peterson, B. M. 2001, arXiv preprint astro-ph/0109495
Reddy, N. A., Kriek, M., Shapley, A. E., et al. 2015, ApJ, 806, 259
Richards, G. T., Lacy, M., Storrie-Lombardi, L. J., et al. 2006, ApJS, 166, 470
Rieke, G. H., & Lebofsky, M. J. 1981, ApJ, 250, 87
Rosario, D. J., Santini, P., Lutz, D., et al. 2012, A&A, 545, A45
Rosario, D. J., Santini, P., Lutz, D., et al. 2013, ApJ, 771, 63
Rosario, D. J., McIntosh, D. H., van der Wel, A., et al. 2015, A&A, 573, A85
Sanders, R. L., Shapley, A. E., Kriek, M., et al. 2016, ApJ, 816, 23
Santini, P., Rosario, D. J., Shao, L., et al. 2012, A&A, 540, A109
Sartori, L. F., Schawinski, K., Treister, E., et al. 2015, MNRAS, 454, 3722
Schawinski, K., Simmons, B. D., Urry, C. M., Treister, E., & Glikman, E. 2012, MNRAS, 425, L61
Schawinski, K., Treister, E., Urry, C. M., et al. 2011, ApJL, 727, L31
Shapley, A. E., Reddy, N. A., Kriek, M., et al. 2015, ApJ, 801, 88
Sharples, R., Bender, R., Agudo Berbel, A., et al. 2013, Msngr, 151, 21
Shivaei, I., Reddy, N. A., Shapley, A. E., et al. 2015, ApJ, 815, 98
Silverman, J. D., Green, P. J., Barkhouse, W., et al. 2008, ApJ, 679, 118
Silverman, J. D., Katarina Kovač, K., Knobel, C., et al. 2009, ApJ, 695, 171
Skelton, R. E., Whitaker, K. E., Momcheva, I. G., et al. 2014, ApJS, 214, 24
Stanley, F., Harrison, C. M., Alexander, D. M., et al. 2015, MNRAS, 453, 591
Steidel, C. C., Rudie, G. C., Strom, A. L., et al. 2014, ApJ, 795, 165

Stern, D., Eisenhardt, P., Gorjian, V., et al. 2005, ApJ, 631, 163
Sutherland, W., & Saunders, W. 1992, MNRAS, 259, 413
Tanaka, M. 2012, PASJ, 64, 36
Treister, E., Schawinski, K., Urry, C. M., & Simmons, B. D. 2012, ApJL, 758, L39
Trouille, L., & Barger, A. J. 2010, ApJ, 722, 212
Trump, J. R., Konidaris, N. P., Barro, G., et al. 2013, ApJL, 763, L6
Trump, J. R., Sun, M., Zeimann, G. R., et al. 2015, ApJ, 811, 26
Ulrich, M. H., Maraschi, L., & Urry, M. 1997, ARA&A, 35, 445
Vasudevan, R. V., & Fabian, A. C. 2007, MNRAS, 381, 1235
Veilleux, S., & Osterbrock, D. E. 1987, ApJS, 63, 295
Vignali, C., Alexander, D. M., Gilli, R., & Pozzi, F. 2010, MNRAS, 404, 48
Whitaker, K. E., van Dokkum, P. G., Brammer, G., & Franx, M. 2012, ApJL, 754, L29
Whitaker, K. E., Labbé, I., van Dokkum, P. G., et al. 2011, ApJ, 735, 86
Wild, V., Heckman, T., & Charlot, S. 2010, MNRAS, 405, 933
Williams, R. J., Quadri, R. F., Franx, M., van Dokkum, P., & Labbé, I. 2009, ApJ, 691, 1879
Williams, R. J., Quadri, R. F., Franx, M., et al. 2010, ApJ, 713, 738
Wong, T. 2009, ApJ, 705, 650
Wright, E. L., Eisenhardt, P. R. M., Mainzer, A. K., et al. 2010, AJ, 140, 1868
Xue, Y. Q., Brandt, W. N., Luo, B., Rafferty, D., et al. 2010, ApJ, 720, 368
Yabe, K., Ohta, K., Iwamuro, F., et al. 2012, PASJ, 64, 60